

**Synthesis and Characterization of a Ferrocene-containing
Aminophenol Ligand: On Route to Redox-switchable Catalysts**

by

© Nhan Duy Pham

A Thesis submitted to the School of Graduate Studies
in partial fulfillment of the requirements for the degree of

Master of Science

in

Department of Chemistry

Memorial University of Newfoundland

St. John's, Newfoundland and Labrador, Canada

December 2023

Abstract

Ferrocene is an organometallic compound classified as a metallocene with the formula $\text{Fe}(\eta^5\text{-C}_5\text{H}_5)_2$. In the latter half of the 1950s, it was discovered and became a "hot" molecule because of its reversible redox behaviour. A number of scientific papers related to ferrocene-based ligands and their applications have been published, and this literature is reviewed in Chapter 1. Scientists have applied them to various fields such as catalysis, heavy metal removal, organic pollutant removal, bio-sensing, food analysis, and energy storage. In 2006 the first example of a redox controlled ring-opening polymerization was reported by Long and coworkers, showing different activities in the polymerization of *rac*-lactide depending on the oxidation state of the ferrocene units.

In this thesis, ferrocene-containing aminophenol ligand which was successfully synthesized and characterized by NMR and UV-Vis spectroscopies, MALDI-TOF mass spectrometry, and X-ray crystallography. The electrochemical behaviour of the ferrocene-containing aminophenol ligand was determined by cyclic voltammetry (CV). These findings provide valuable information for further studies on the potential applications of the synthesized ligand in various fields, such as catalysis and electrochemistry.

Acknowledgments

I am delighted to express my gratitude to Dr. Francesca M. Kerton, my supervisor, for providing me with a life-changing opportunity to work in the exciting field of chemistry. Dr. Kerton's positive attitude and willingness to encourage my ideas without judgment have been instrumental in my academic journey. She has not only motivated me in my research but has also made the past two years of my academic journey enjoyable with her amicable and cheerful personality. Dr. Kerton's patience during individual meetings, scientific writing lessons, assistance with coursework, and demonstrating laboratory procedures have been invaluable in shaping my academic growth. I am grateful for the guidance and support that Dr. Kerton has provided, which has helped me develop into a better researcher. Her dedication to my academic growth has been remarkable, and I will always be thankful for her contribution to my academic success.

I am deeply grateful for the invaluable guidance and support provided by Dr. Chris Kozak throughout my research and academic journey. His astute criticism and insightful advice during group meetings have been instrumental in shaping my ideas and improving the quality of my work. Additionally, his expertise and training on laboratory equipment have been immensely helpful in enhancing my technical skills. Dr. Kozak's unwavering

passion and commitment to chemistry research have been a constant source of inspiration for me, and I feel fortunate to have had the opportunity to work under his mentorship. I cannot thank him enough for his contributions to my growth and development as a researcher.

Next, I express my gratitude to Dr. Jane Stockmann for her valuable input during the committee meetings. I am also thankful to Dr. Celine M. Schneider for her guidance and support with NMR spectra. Dr. Jian-Bin Lin has my appreciation for his help in solving my crystal structures, and I am grateful to Dr. Stefana Egli for providing training with MALDI-TOF MS. Their expertise and assistance have been invaluable in the success of my research.

I would also like to thank NSERC (Dr. Kerton's research grant), Department of Chemistry, School of Graduate Studies (SGS), Graduate Students' Union (GSU), Teaching Assistants' Union of Memorial University of Newfoundland (TAUMUN) and Memorial University of Newfoundland for funding, which was a huge contribution to the successful completion of my master's program.

I would like to extend my gratitude to the former and current members of the Green Chemistry and Catalysis group, who have been instrumental in the success of my work. I would like to give special recognition to Fatma, Dr. Juliana, Sachel, Cyler, Matthew,

Mikhailey, Sara, Olivia, and Sarah B for their invaluable assistance and guidance in the laboratory. Their friendly demeanour and insightful advice have been crucial to my development as a researcher, and I am deeply grateful for their contributions.

In closing, I extend my heartfelt gratitude to my dear family members and friends at Memorial University for their unwavering support throughout my academic journey. Especially, I am particularly grateful to my lover who provided unwavering support and motivation throughout the challenging process of completing my thesis. Their invaluable advice and guidance regarding my research helped me achieve success and I cannot express enough how much I appreciate their contribution. Thank you so much from bottom of my heart.

Table of Contents

Abstract	i
Acknowledgments	ii
Table of Contents	v
List of Tables	viii
List of Figures	x
List of Schemes	xiii
List of Abbreviations and Symbols	xv
Chapter 1: Introduction	1
1.1 Overview of ferrocene	1
1.2 Redox-switchable catalyst	4
1.3 Methods of synthesis of ferrocene-based ligands	12
1.4 Motivation of the research	18
Chapter 2: Experimental Methods	20
2.1 General methods and instrumentation.....	20
2.2 Procedure for the synthesis of 1-ferrocenyl-4-hydroxybenzene	21
2.3 Procedure for the synthesis of a ferrocene-containing aminophenol.....	23

2.4	Calibration and scanning procedure for CV	24
Chapter 3: Results and Discussion		27
3.1	Characterization of compounds' structures.....	27
3.1.1	Characterization of 1-ferrocenyl-4-hydroxybenzene	27
3.1.1.1	¹ H-NMR spectroscopy	28
3.1.1.2	¹³ C-NMR spectroscopy	30
3.1.2	Characterization of a ferrocene-containing aminophenol.....	34
3.1.2.1	¹ H-NMR spectroscopy	34
3.1.2.2	¹³ C-NMR spectroscopy	37
3.1.2.3	MALDI-TOF mass spectrometry	41
3.1.2.4	X-ray crystallography	44
3.1.2.5	UV-Vis spectroscopy	50
3.2	Electrochemical behaviour of compounds.....	53
3.2.1	Cyclic voltammetry (CV).....	53
3.2.2	Electrochemical behaviour of ferrocene	54
3.2.3	Electrochemical behaviour of 1-ferrocenyl-4-hydroxybenzene	56
3.2.4	Electrochemical behaviour of a ferrocene-containing aminophenol	60
3.3	Reaction mechanism	65
3.3.1	Mechanism of synthesis of 1-ferrocenyl-4-hydroxybenzene.....	65
3.3.2	Mechanism of synthesis of a ferrocene-containing aminophenol.....	67
Chapter 4: Conclusions and Future Work.....		69

References 72

Appendix 80

List of Tables

Table 1.1 Selected of 4-ferrocenylquinoline derivatives developed by Mou and co-worker.	15
Table 1.2 Selected of ferrocenyl chalcones synthesized by Montes-Gonzalez and coworkers.....	17
Table 3.1 Table of ^1H -NMR signals of compound 1	28
Table 3.2 Table of ^{13}C -NMR signals of compound 1	30
Table 3.3 Table of ^1H -NMR signals of compound 2	34
Table 3.4 Table of ^{13}C -NMR signals of compound 2	37
Table 3.5 Crystal data and structure refinement.....	47
Table 3.6 Calculation of the hydrogen bonding among 3 elements: O, H, N (Van der Waals radii of Nitrogen (N)=1.55 Å, Hydrogen (H) = 1.20 Å, Oxygen (O) = 1.52 Å).....	49
Table 3.7 The calculation of half-wave potential of ferrocene.	56
Table 3.8 The calculation of half-wave potential of compound 1 versus Fc^+/Fc	58
Table 3.9 The calculation of half-wave potential of compound 2 versus Fc^+/Fc	62
Table 3.10 The calculation and summarize of the half-wave potential of ferrocene, compound 1 , compound 2 before and after correction (versus Fc^+/Fc).	64
Table A.1 The elemental analysis of compound 2 ($\text{C}_{40}\text{H}_{36}\text{Fe}_2\text{N}_2\text{O}_2$).	83
Table A.2 Fractional Atomic Coordinates ($\times 10^4$) and Equivalent Isotropic Displacement Parameters ($\text{Å}^2 \times 10^3$). U_{eq} is defined as 1/3 of the trace of the orthogonalised U_{IJ} tensor.	84
Table A.3 Selected Bond Distances (Å).....	87

Table A.4 Selected Bond Angles.	89
Table A.5 Selected Torsion Angles.....	93

List of Figures

Figure 1.1 The structure of ferrocene.....	2
Figure 1.2 The structure of [(salen)Fc ₂]Ti(O ⁱ Pr) ₂	7
Figure 1.3 A plot of conversion versus time for polymerization of rac-lactide. Figure reproduced and reprinted from Journal of the American Chemical Society 128 , 7410-7411 (2006) with permission from American Chemical Society.	8
Figure 1.4 Structure of acetyl ferrocenium tetrakis(3,5-bis(trifluoromethyl)phenyl)borate (AcFcBAR ^F).	10
Figure 1.5 ¹ H-NMR spectrum for different stages in one-pot ring-opening copolymerization reaction of LA and CL. Figure reproduced and reprinted from Journal of the American Chemical Society 136 , 11264-11267 (2014) with permission from American Chemical Society.	11
Figure 3.1 The chemical structure of compound 1 . Chemical formula: C ₁₆ H ₁₄ FeO, molecular weight: 278.04 g/mol, R _f value = 0.22 (hexane: acetone), appearance: orange powder.....	27
Figure 3.2 ¹ H-NMR spectrum of compound 1	30
Figure 3.3 ¹³ C-NMR spectrum of compound 1	33
Figure 3.4 The chemical structure of compound 2 . Chemical formula: C ₄₀ H ₃₆ Fe ₂ N ₂ O ₂ , molecular weight: 688.14 g/mol, melting point: 170 °C, appearance: yellow powder.....	34
Figure 3.5 ¹ H-NMR spectrum of compound 2	37
Figure 3.6 ¹³ C-NMR spectrum of compound 2	40

Figure 3.7 The structure of anthracene.	42
Figure 3.8 MALDI-TOF MS spectrum of compound 2 dissolved in dichloromethane, CH ₂ Cl ₂ and were thus combined with anthracene (also soluble) as a matrix in a 1:1 ratio at the positive mode.	43
Figure 3.9 X-ray crystal structure of compound 2 (non-hydrogen atoms are represented by displacement ellipsoids at the 30% probability level).	45
Figure 3.10 The comparison UV-Vis spectrum of ferrocene, compound 1 , and compound 2 , diluted in dichloromethane (DCM) at the concentration of 5 mM (room temperature).	51
Figure 3.11 The cyclic voltammogram of ferrocene (5 mM) was recorded in dichloromethane (DCM) of solution of tetra-n-butylammonium hexafluorophosphate [nBu ₄ N][PF ₆] (0.1 M). Scan rate: 100 mV/s.	55
Figure 3.12 The cyclic voltammogram of compound 1 (5 mM) was recorded in dichloromethane (DCM) of solution of tetra-n-butylammonium hexafluorophosphate [nBu ₄ N][PF ₆] (0.1 M). Scan rate: 100 mV/s. Potential versus Fc ⁺ /Fc.	57
Figure 3.13 The cyclic voltammogram of compound 2 (5 mM) was recorded in dichloromethane (DCM) of solution of tetra-n-butylammonium hexafluorophosphate [nBu ₄ N][PF ₆] (0.1 M). Scan rate: 100 mV/s. Potential versus Fc ⁺ /Fc.	61
Figure 4.1 Example of possible complex with ferrocene containing aminophenolate ligand derived from compound 2	71
Figure A.1 Procedure for setting up the CV experiment.	80
Figure A.2 The different colour of ferrocene, compound 1 , and compound 2 when they are diluted in dichloromethane (DCM) at the concentration of 5 mM (room temperature).	81

Figure A.3 The different colour of ferrocene, compound **1**, and compound **2** in solid state at room temperature.82

List of Schemes

Scheme 1.1 Reversible one-electron oxidation of ferrocene.....	3
Scheme 1.2 The first instance of redox-mediate ring-opening polymerization (ROP).....	6
Scheme 1.3 Ring-opening polymerization of rac-lactide.	7
Scheme 1.4 Optimization of redox switchable copolymerization of L-lactide and ϵ -caprolactone (1.1; 1.0 M in benzene) with (thiofan*)Ti(O ⁱ Pr) ₂ at 100 °C.....	9
Scheme 1.5 Conversion of (thiofan*)Ti(O ⁱ Pr) ₂ to its oxidized state.....	10
Scheme 1.6 Reaction of synthesis of 2,5-bis(2-ferrocenyl-6-methylpyridin-4-yl)-thiophene.....	12
Scheme 1.7 Synthesis of β -ketoenamide (X) by reaction of ferrocenecarboxylic acid amide with acetylacetone followed by cyclocondensation and <i>O</i> -nonaflation to give pyrid-4-yl nonaflate (Y). Reaction and conditions: (a) <i>p</i> -toluenesulfonic acid, toluene, reflux, 5 h; (b) trimethylsilyl trifluoromethanesulfonate, NEt ₃ , 1,2-dichloroethane, 80 °C, 48 h; (c) NaH, nonafluorobutanesulfonyl fluoride, THF, room temperature, 24 h.....	13
Scheme 1.8 The reaction of synthesis of ferrocene-functional thiophene derivative.....	14
Scheme 1.9 Synthesis of ferrocene carboxaldehyde.	16
Scheme 1.10 Synthesis of ferrocenylterpyridine ligand.....	16
Scheme 1.11 The reaction of synthesis of ferrocenyl chalcones.....	17
Scheme 3.1 Proposed mechanism for electrochemical redox of compound 1 via cyclic voltammogram.	59

Scheme 3.2 Proposed mechanism for electrochemical redox of compound 2 via cyclic voltammogram.	63
Scheme 3.3 The mechanism of synthesis of compound 1	66
Scheme 3.4 The mechanism of synthesis of compound 2	68

List of Abbreviations and Symbols

et al.	and others
Å	Ångstrom (10^{-10} m)
amu	atomic mass unit
salan	N,N'-bis(phenolato)-1,2-diaminoethane
salen	N,N'-bis(salicylaldehydo)ethylenediamine
salalen	a combination of salan and salen ligands
cm	centimetre (10^{-2} m)
J	coupling constant
(°)	degree
s	singlet
d	doublet
dd	doublet of doublet
CL	ϵ -caprolactone
DMF	dimethylformamide
Et	ethyl
Me	methyl
MeOH	methanol
g	gram
h	hour(s)

in situ	“in the reaction mixture”
LA	L-lactide
MS	mass spectrometry
m/z	mass-to-charge ratio
MALDI-TOF	matrix assisted laser desorption/ionization time-of-flight
μL	microlitre (10^{-6} L)
mmol	millimole (10^{-3} mol)
min	minute
M	molar (mol/L)
NMR	nuclear magnetic resonance
M_n	number average molecular weight
<i>trans</i>	“on the other side”
<i>cis</i>	“on the same side”
ppm	parts per million
Ph	phenyl
PCL-PLA	(poly L-lactide)-(poly caprolactone)
PPC	poly(propylene carbonate)
PC	propylene carbonate
PO	propylene oxide
ROP	ring-opening polymerization
SO	styrene oxide

tBu	tertiary-butyl
THF	tetrahydrofuran
TMS	tetramethylsilane
TOF	turnover frequency
TON	turnover number
UV-Vis	ultraviolet-visible
vs	versus
M_w	weight average molecular weight
CV	cyclic voltammogram

Chapter 1: Introduction

1.1 Overview of ferrocene

Ferrocene was discovered by P. L. Pauson and J. T. Kealy in 1951¹ as a compound that consists of an iron atom sandwiched between two parallel C₅H₅-rings. Its structure was elucidated by Robert Burns Woodward and Geoffrey Wilkinson in 1952.² Woodward and Rosenblum's paper, the structure and chemistry of ferrocene, as described and published in the Journal of the American Chemical Society, is considered a seminal work in the field of organometallic chemistry (**Figure 1.1**).³ However, Fischer made significant contributions to the study of ferrocene, including the synthesis of a variety of ferrocene derivatives, which earned ferrocene its nickname as the "sandwich" compound. Fischer and his colleagues were awarded the Nobel Prize in Chemistry in 1973 for their work on the development of organometallic chemistry, which led to a surge of research in the field.⁴

Over the last few decades, the study of ferrocene and its derivatives has rapidly developed,^{5,6} and scientists have taken advantage of these compounds for various applications in electrochemistry,⁷ medicinal chemistry,^{8,9} and material chemistry.¹⁰ The discovery of ferrocene has led to a deeper understanding of organometallic chemistry and has opened up new avenues for research in this field.

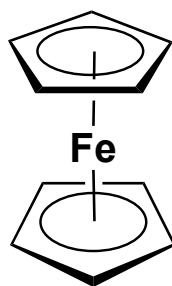
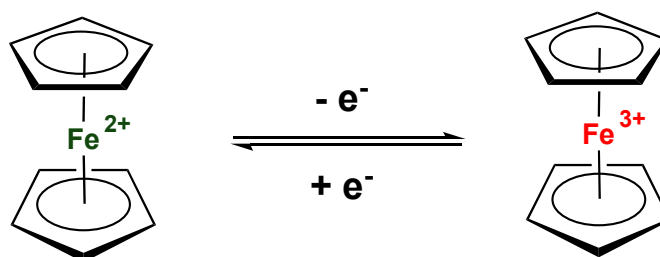


Figure 1.1 The structure of ferrocene.

Ferrocene is a particularly important compound due to its unique electronic and structural properties. It has been found to be an excellent electron donor, and its electronic properties can be finely tuned by varying the substituents on the cyclopentadienyl rings. This makes it a useful compound in electrochemistry, where it is used as a reference material for measuring the redox potentials of other compounds. Ferrocene and its derivatives have also found applications in the field of organic synthesis, where they can be used as reagents for a variety of chemical reactions.^{11,12}

In addition to its applications in electrochemistry and organic synthesis, ferrocene and its derivatives have also shown promise in the field of medicinal chemistry. For example, ferrocene-containing compounds have been found to exhibit anti-cancer activity, and several ferrocene-based drugs are currently in clinical trials. Ferrocene and its derivatives have also been investigated as potential antibacterial and antifungal agents.¹³⁻

The unique structure of ferrocene has also made it a popular choice for the development of new materials. Ferrocene-containing polymers and materials have been synthesized, which exhibit interesting electronic, magnetic, and optical properties. These materials have potential applications in the development of new electronic devices, such as sensors and transistors.¹⁷⁻²¹



Scheme 1.1 Reversible one-electron oxidation of ferrocene.

Despite the significant progress that has been made in the study of ferrocene and its derivatives, there is still much to be learned about these compounds. For example, the mechanism by which ferrocene-based drugs exert their anti-cancer activity is not fully understood, and there is still much to be learned about the electronic and magnetic properties of ferrocene-containing materials. As such, research in this area continues to be an active and exciting field of study.¹⁴⁻¹⁶

Recently, due to its electronic characteristics, the ferrocene moiety has played a crucial role in the backbone as a substituent in auxiliary ligands in coordination chemistry

which is the study of the interaction of metals and carbon. Moreover, the iron center readily undergoes a reversible one-electron oxidation to convert ferrocene to ferrocenium and this ion can modulate reactivity (**Scheme 1.1**).²²

1.2 Redox-switchable catalyst

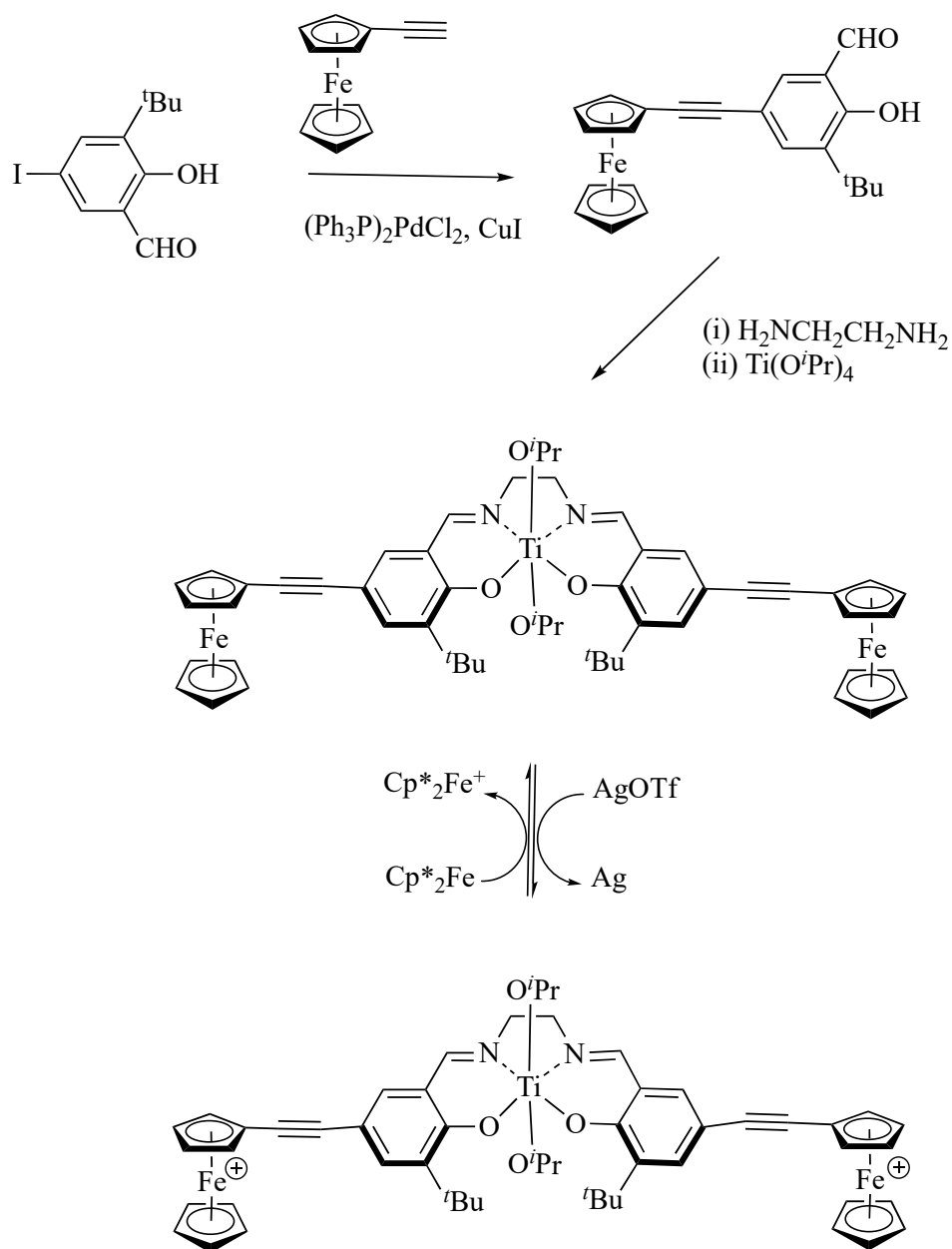
Organometallic compounds refer to chemical compounds that contain metal-carbon bonds.²³ Some organometallic compounds that have been investigated for their reversible reactivity. These compounds can undergo reversible redox reactions, making them promising candidates for the development of electrocatalytic processes.²⁴ Redox-switchable catalysts are an innovative type of catalyst that offer a novel way of modulating the reactivity of transition metal complexes by altering their electronic properties. The basic idea behind these catalysts is to use a redox-active ligand, which can switch between its oxidized and reduced states, to modulate the electron-donating or -withdrawing nature of the coordinated ligand. By doing so, the catalytic activity of the transition metal can be influenced, making redox-switchable catalysts an attractive option for a wide range of applications.^{25,26} One of the most promising applications of redox-switchable catalysts is in electrocatalysis. By modulating the redox state of the ligand, the catalyst can be used to selectively promote or inhibit different electrochemical reactions, making it a versatile tool for applications such as energy storage and conversion. For example, redox-switchable

catalysts have been used to selectively promote the reduction of CO₂ to CO in electrochemical cells, which has significant potential for renewable energy applications.²⁷ In addition to electrocatalysis, redox-switchable catalysts have also been explored in other fields such as photochemistry, where they can be used to modulate the activity of light-sensitive transition metal complexes,^{28,29} and biology, where the redox state of the ligand can be used to modulate the activity of enzymes, receptors, and other biological molecules.³⁰⁻³³

Ferrocene and its derivatives have been used in redox-switchable homogeneous catalysts for several reactions including ring-opening polymerizations and ring-closing metathesis. Due to its adaptability, simplicity in functionalization and reversible oxidation process, it is frequently used as the redox-active molecule in such catalysts.³⁴⁻⁴⁰ Redox-switchable ring-opening polymerization (ROP), which is a powerful technique for synthesizing biodegradable copolymers, has received a lot of attention in the field of switchable catalysis since it was first discovered by N. Long's research group in 2006 (**Scheme 1.2**). First, a coupling reaction catalyzed by PdCl₂(PPh₃)₂/CuI was utilized to produce salicylaldehyde with an ethynylferrocene substituent. Subsequently, it underwent a reaction with ethylenediamine and Ti(OⁱPr)₄, resulting in the formation of [(salen)Fc₂]Ti(OⁱPr)₂. Finally, this compound was subjected to oxidation through a reaction

with AgOTf, and the resulting product was reduced by reacting it with Cp*₂Fe to yield

[(salen)Fc₂Ti(OⁱPr)₂].⁴¹



Scheme 1.2 The Synthesized route and redox-switchable reaction of [(salen)Fc₂Ti(OⁱPr)₂].

They investigated that changing the oxidation state of the ferrocenyl unit in $[(\text{salen})\text{Fc}_2]\text{Ti}(\text{O}^i\text{Pr})_2$ (**Figure 1.2**) is able to modify the rate of *rac*-lactide ring-opening polymerization (**Scheme 1.3**).⁴¹

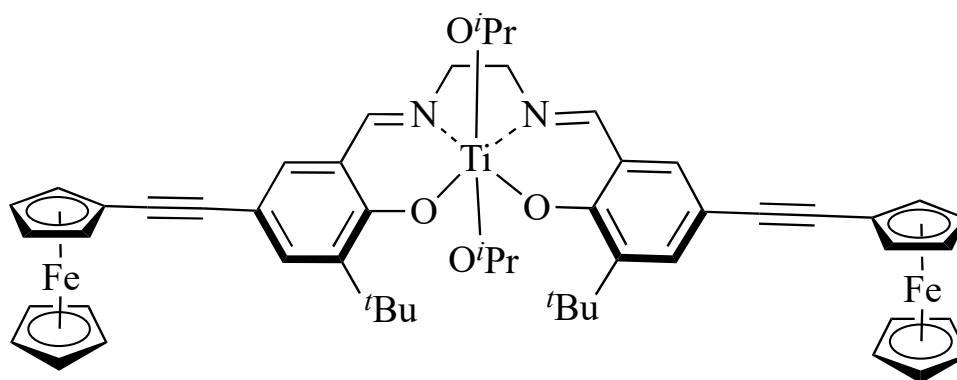
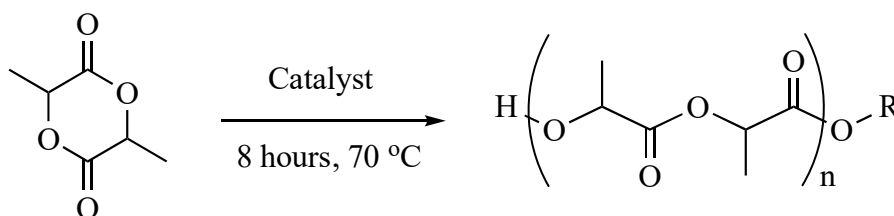


Figure 1.2 The structure of $[(\text{salen})\text{Fc}_2]\text{Ti}(\text{O}^i\text{Pr})_2$.



Scheme 1.3 Ring-opening polymerization of *rac*-lactide.

After 8 hours at 70 °C, the titanium center polymerized *rac*-lactide with an 18% monomer conversion when the ferrocene compound was in its reduced Fe(II) form. Additionally, it could be seen that when they used AgOTf to oxidize the ferrocene group,

there was a significant decrease in reactivity (**Figure 1.3**). Subsequently, the catalytic reactivity could be restored when using FeCp_2^* to reduce Fe(III) back to Fe(II) .⁴¹

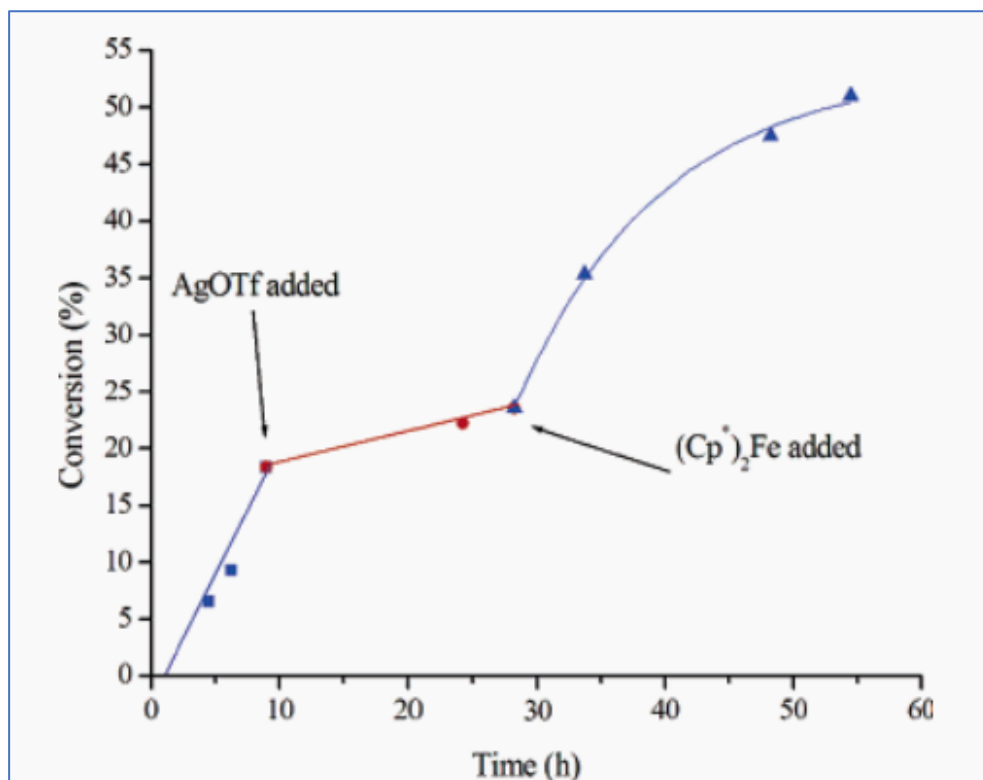
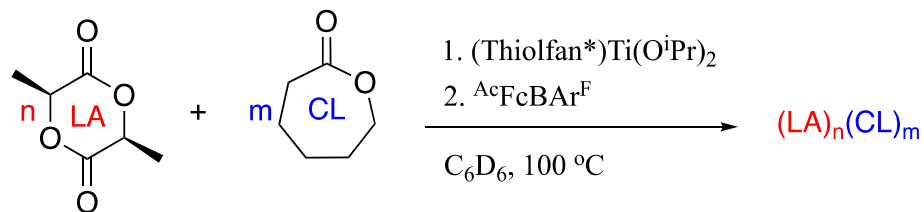


Figure 1.3 A plot of conversion versus time for polymerization of *rac*-lactide. Figure reproduced and reprinted from Journal of the American Chemical Society **128**, 7410-7411 (2006) with permission from American Chemical Society.

Copolymer (poly L-lactide)-(poly caprolactone), abbreviated as PCL-PLA, was successfully synthesized via one-pot copolymerization of L-lactide (LA) and ϵ -

caprolactone (CL) using (thiofan*)Ti(OⁱPr)₂ as a redox-switchable catalyst (**Scheme 1.4**).⁴²



Scheme 1.4 The reaction of redox switchable copolymerization of L-lactide and ε-caprolactone (1.1; 1.0 M in benzene) with (thiofan*)Ti(OⁱPr)₂ at 100 °C.

Initially, 58% conversion of LA was observed at 100 °C for 36 hours with the reduced form of initiator, ε-caprolactone was not polymerized at this point (**Scheme 1.5**). Then in order to convert the catalyst into an oxidized form, they introduced the oxidant: acetyl ferrocenium tetrakis(3,5-bis(trifluoromethyl)phenyl) borate (^{Ac}FcBAr^F). The structure of ^{Ac}FcBAr^F is shown in **Figure 1.4**.

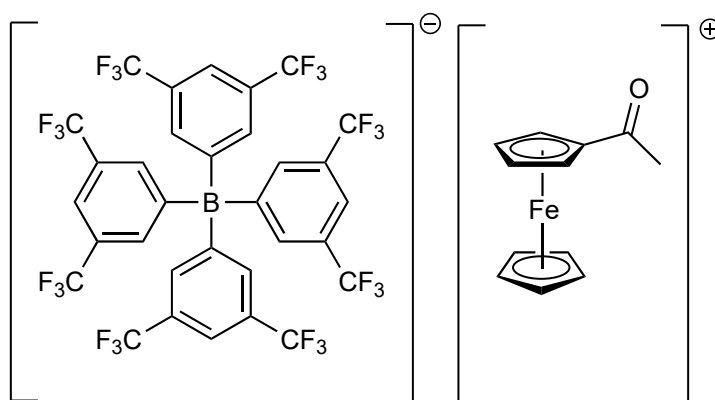
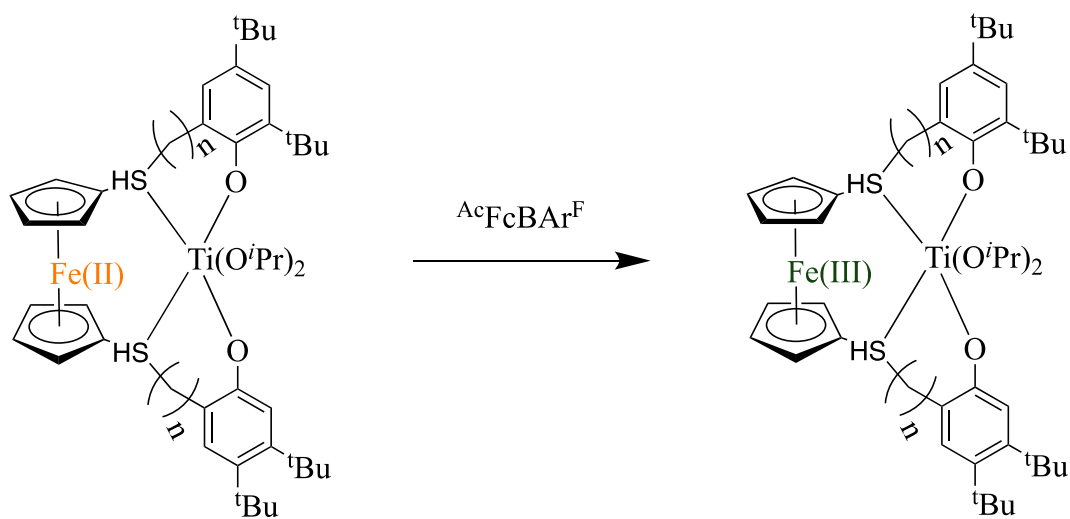


Figure 1.3 Structure of acetyl ferrocenium tetrakis(3,5-bis(trifluoromethyl)phenyl)borate ($^{\text{AcFc}}\text{BAR}^{\text{F}}$).



Scheme 1.5 Conversion of (thiolfan*) $\text{Ti}(\text{O}^{\text{iPr}})_2$ to its oxidized state.

After 2 hours, there was no increase in conversion of LA, while ϵ -caprolactone was polymerized with 18% conversion.⁴² This process was monitored by $^1\text{H-NMR}$ spectroscopy

to detect the proton signals of these polymers and how does monitoring the $^1\text{H-NMR}$ control copolymer formation (**Figure 1.5**).

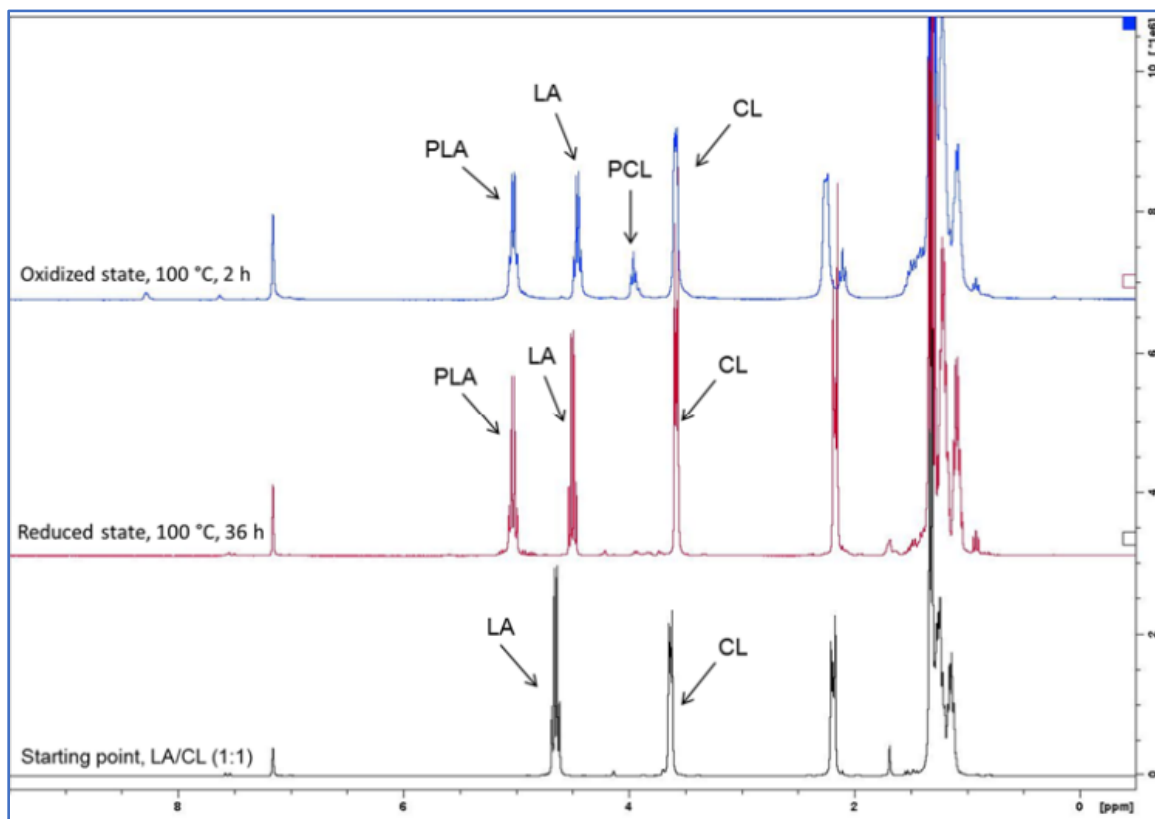
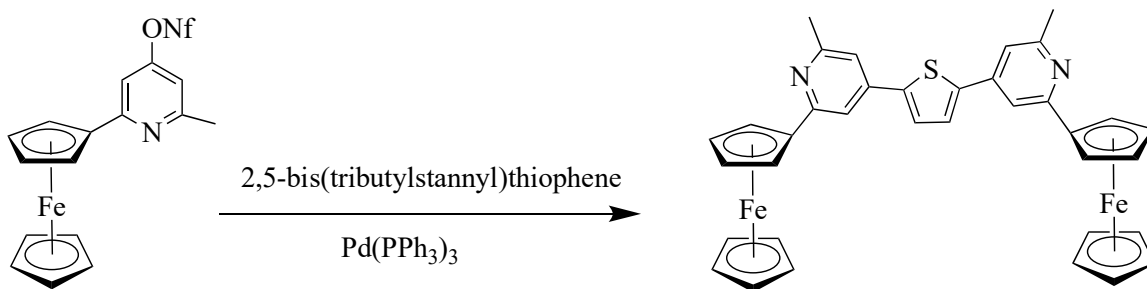


Figure 1.4 $^1\text{H-NMR}$ spectrum for different stages in one-pot ring-opening copolymerization reaction of LA and CL. Figure reproduced and reprinted from Journal of the American Chemical Society **136**, 11264-11267 (2014) with permission from American Chemical Society.

1.3 Methods of synthesis of ferrocene-based ligands

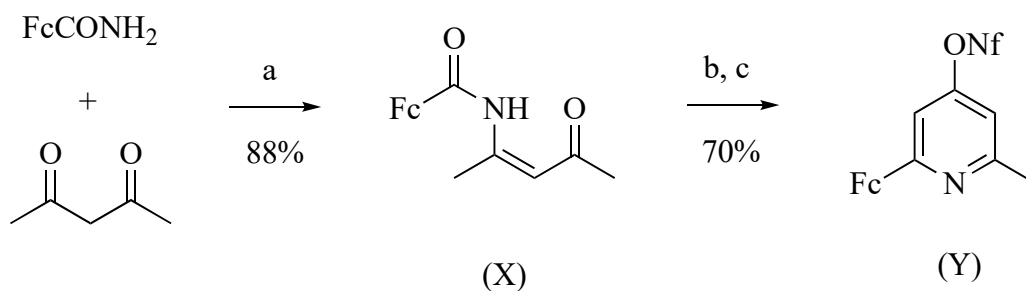
In 2015, Gabriel and his colleagues presented a novel approach to synthesize 2,5-bis(2-ferrocenyl-6-methylpyridin-4-yl)thiophene using a Stille coupling reaction with acetonitril in 24 hours at 60 °C (**Scheme 1.6**).⁴³



Scheme 1.6 Reaction of synthesis of 2,5-bis(2-ferrocenyl-6-methylpyridin-4-yl)-thiophene.

The procedure to synthesize the starting ligand material pyrid-4-yl nonaflate is described in **Scheme 1.7**. The reaction utilized pyrid-4-yl nonaflate and 2,5-bis(tributylstannyl)thiophene as starting materials and was carried out in *N,N*-dimethylformamide (DMF) at 90 °C for a period of 2 hours. The reaction was catalyzed by Pd(Ph)₃, which served as a source of palladium ions, and the resulting product was obtained with a high yield of 90%. The product, 2,5-bis(2-ferrocenyl-6-methylpyridin-4-yl)thiophene, is a valuable intermediate in the synthesis of various organic materials,

including polymers and electronic materials. This process resulted in the formation of the desired product, which was isolated and purified by standard methods.⁴³



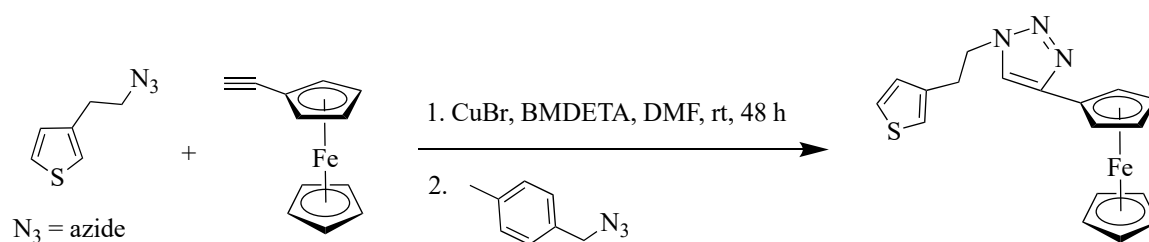
Scheme 1.7 Synthesis of β -ketoenamide (X) by reaction of ferrocenecarboxylic acid amide with acetylacetone followed by cyclocondensation and *O*-nonaflation to give pyrid-4-yl nonaflate (Y). Reaction and conditions: (a) *p*-toluenesulfonic acid, toluene, reflux, 5 h; (b) trimethylsilyl trifluoromethanesulfonate, NEt₃, 1,2-dichloroethane, 80 °C, 48 h; (c) NaH, nonafluorobutanesulfonyl fluoride, THF, room temperature, 24 h.

Karagollu and colleagues developed a reaction that utilizes a Cu(I) salt as a catalyst to synthesize a ferrocene-functionalized thiophene derivative.⁴⁴ The reaction involves the combination of 3-(2-azidoethyl)thiophene and ethynylferrocene in DMF at room temperature for 48 hours, as shown in **Scheme 1.8**. The reaction is a significant advancement in the field of organic synthesis, as it offers a straightforward and efficient method for the synthesis of ferrocene-functionalized thiophene derivatives. The Cu(I) salt catalyst used in the reaction is known for its ability to facilitate the coupling of terminal

alkynes and azides through a process known as “click chemistry” (Nobel Prize 2022).⁴⁵

The high yield of 87.4% obtained in the reaction indicates its efficiency and selectivity.⁴⁴

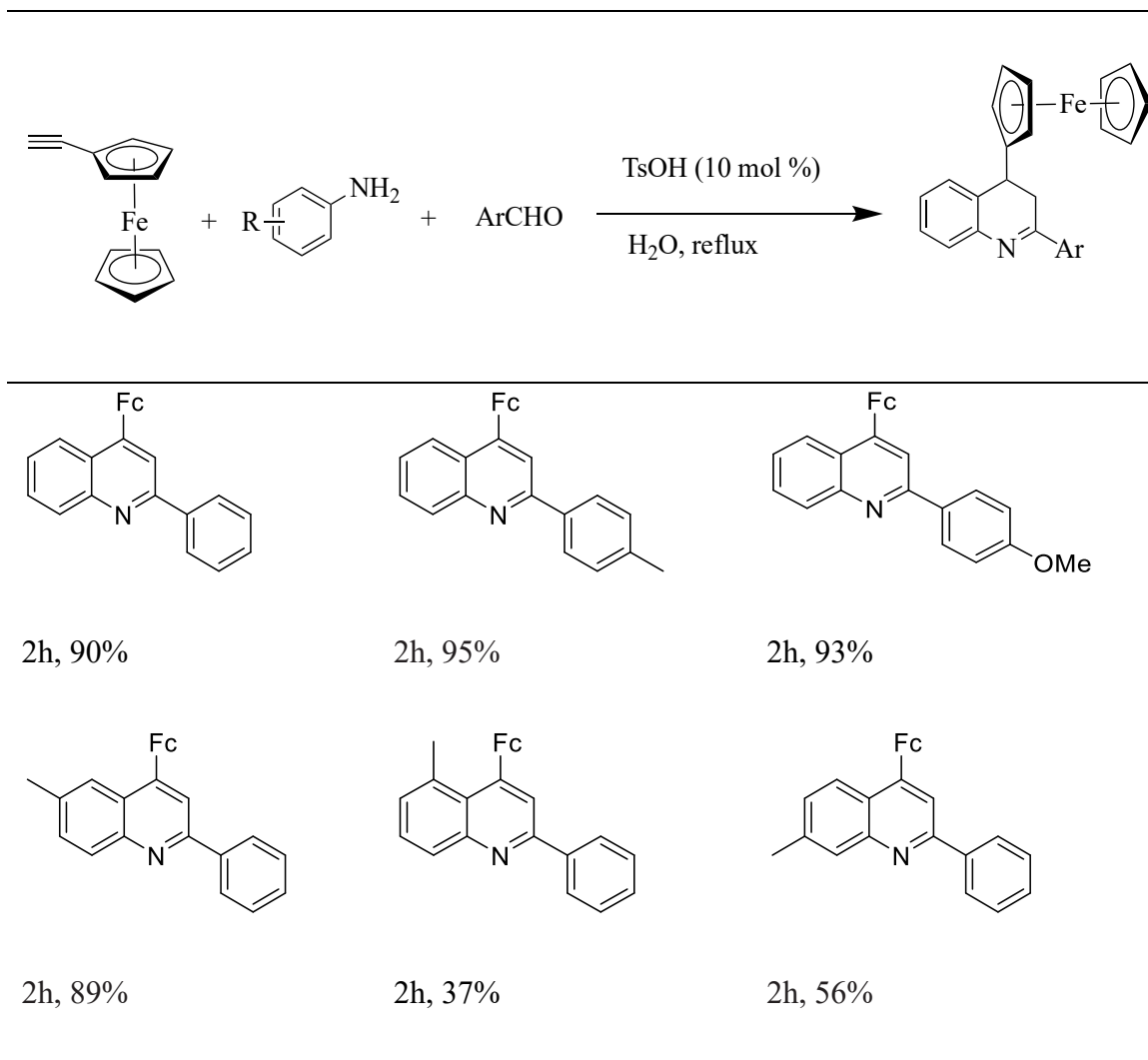
The product obtained can be used in a variety of applications, including organic electronics, optoelectronics, and materials science.



Scheme 1.8 The reaction of synthesis of ferrocene-functional thiophene derivative.

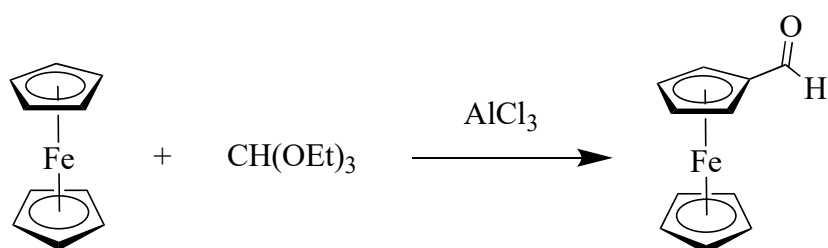
The development of environmentally friendly catalysts has become increasingly important in organic synthesis due to the harmful effects of metal catalysts. Researchers have been exploring alternative methods to reduce the usage of these detrimental catalysts as much as possible. In 2018, Rui-Qi Mou and his colleagues developed a novel approach to synthesize 4-ferrocenylquinoline derivatives using tosylic acid (TsOH) as an organic catalyst in a three-compound reaction.⁴⁶ This approach utilized simple starting materials such as amine, aromatic aldehyde, and ferrocenylacetylene in water. The results showed that the products were obtained with very high yields of 69-95% (**Table 1.1**), which demonstrated the effectiveness of the new method.

Table 1.1 Selected of 4-ferrocenylquinoline derivatives developed by Mou and co-worker.

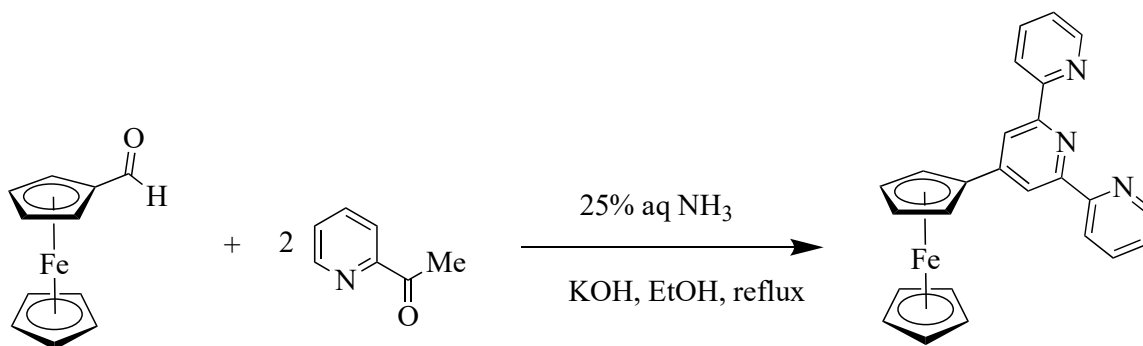


In 2016, a ferrocene containing terpyridine ligand was reported by Hayat and co-worker.⁴⁷ The reaction began with the condensation of 2-acetylpyridine and ferrocene carboxaldehyde which is synthesized from ferrocene and triethyl orthoformate with $AlCl_3$ as a catalyst (**Scheme 1.9**).⁴⁸ The aldehyde formed was then subjected to a Michael addition reaction with a second equivalent of 2-acetylpyridine with the presence of ammonia. The

reaction resulted in the formation of the central pyridine ring, which is a key component of many important organic compounds. The one-pot synthesis method used in this reaction is a straightforward and efficient approach for the synthesis of pyridine derivatives. This method can be used to synthesize a wide range of pyridine-based compounds with different functional groups and substituents.



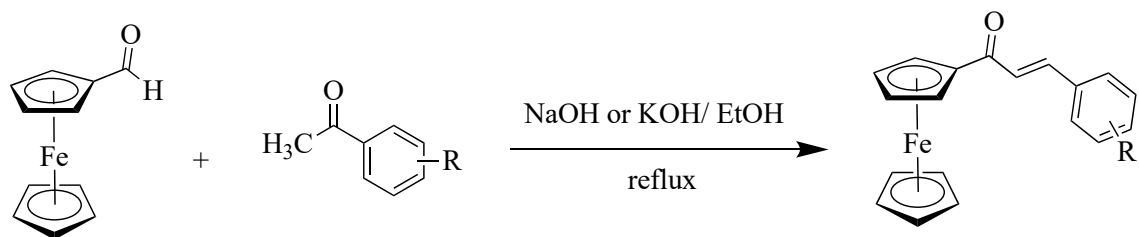
Scheme 1.9 Synthesis of ferrocene carboxaldehyde.



Scheme 1.10 Synthesis of ferrocenylterpyridine ligand.

A strategy for synthesis of ferrocenyl chalcone was investigated by Montes-Gonzalez and coworkers in 2019 (**Scheme 1.11**).⁴⁹ They utilized Claisen-Schmidt condensation catalyzed by base in solvent-free condition or in water to synthesize

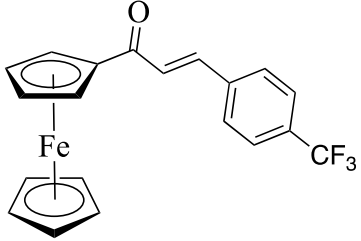
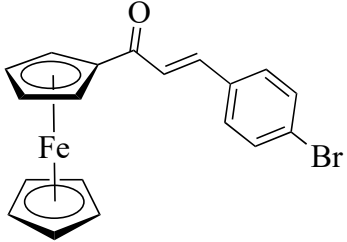
ferrocenyl chalcone from ferrocenylcarbaldehyde and acetophenone derivatives. Their research's results revealed that they obtained products with high yield (**Table 1.2**).



Scheme 1.11 Synthesis reaction for ferrocenyl chalcones.

Table 1.2 Selected of ferrocenyl chalcones synthesized by Montes-Gonzalez and coworkers.

R	Conditions and Time	Yield (%)
	NaOH, EtOH, 10 min	96
	KOH, EtOH, 12 h	85

	KOH, EtOH, 5 h	49
	NaOH, EtOH, 10 min	98

1.4 Motivation of the research

In recent years, the synthesis of ferrocene-containing ligands has gained significant attention in the field of chemistry due to their various useful applications in everyday life. Various methods for synthesizing ferrocenyl ligands have been developed, each with their own benefits and drawbacks. Despite this, the demand for novel ferrocene ligands has not been satisfied, as new compounds with different properties are constantly needed to meet the demands of modern technology.

One approach to synthesizing new ferrocene ligands is through a modified Mannich reaction, which involves the condensation of an amine, an aldehyde, and a phenol. This reaction has been widely utilized in the synthesis of complex organic molecules due to its

mild reaction conditions, simple procedure, and high yields. Therefore, our motivation is to use the Mannich reaction to synthesize a new ferrocene-based ligand.

Our proposed ligand has potential applications as a redox-switchable catalyst. Redox-switchable catalysts are a class of catalysts that can be reversibly activated and deactivated by changing their oxidation state, which can be achieved through the application of an electric potential. This makes them useful in catalyzing reactions that require precise control over the reaction rate and selectivity. Therefore, our goal is not only to synthesize a new ferrocene-based ligand but also to characterize its electrochemical properties by cyclic voltammetry, with the aim of using it as a redox-switchable catalyst for further research.

Chapter 2: Experimental Methods

2.1 General methods and instrumentation

All manipulations were performed in air. Reagents were purchased from Sigma-Aldrich or Fisher Scientific and used as received. NMR spectra were recorded at 300 MHz for ^1H and 75.5 MHz for ^{13}C . CDCl_3 was purchased from Cambridge Isotope Laboratories and used as received. Elemental analyses were performed at Saint Mary's University, Halifax, Nova Scotia, Canada. UV-Vis spectroscopy was performed using an Ocean Optics USB4000 spectrometer in 1 cm quartz cuvettes. Melting points were measured using the OptiMelt MPA100 Automated Melting Point System Instrument at Memorial University of Newfoundland, St. John's, Canada. MALDI-TOF mass spectrometry was obtained on a Bruker ultrafleXtreme mass spectrometer using anthracene matrix. Electrochemical measurements were carried out using PINE research electrochemical potentiostat instrument. Single-crystal X-ray diffraction was performed by Dr. J. B. Lin (C-CART, Memorial University of Newfoundland). X-ray diffraction data were collected at 100(2) K on a XtaLAB Synergy-S diffractometers using Cu $K\alpha$ radiation ($\lambda = 1.5406 \text{ \AA}$). The crystal was mounted on nylon CryoLoops with Paratone-N oil. The data collection and reduction were processed within CrysAlisPro (Rigaku OD, 2021). A multi-scan absorption correction

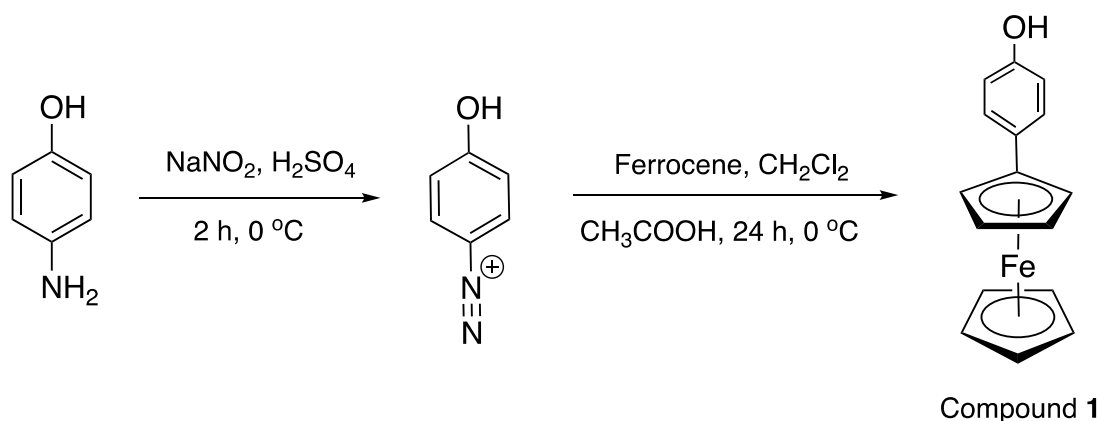
was applied to the collected reflections. Using Olex2,⁵⁰ the structure was solved with the ShelXT⁵¹ structure solution program using Intrinsic Phasing and refined with the ShelXL⁵² refinement package using Least Squares minimisation. All non-hydrogen atoms were refined anisotropically. The hydroxyl hydrogen atoms in the compound were located in different Fourier maps and refined using the DFIX and HTAB commands. All other organic hydrogen atoms were generated geometrically.

2.2 Procedure for the synthesis of 1-ferrocenyl-4-hydroxybenzene

Synthesis of 1-ferrocenyl-4-hydroxybenzene (denoted as compound **1**) following the procedure of Sumner and Creager (**Scheme 2.1**).⁵³ 1 equivalent of 4-aminophenol (5.46 g, 50.0 mmol) was dissolved in 60 mL of 20% sulfuric acid in a 250 mL two-neck round-bottom flask. The solution was cooled to 0 °C in an ice bath. Then, 2 equivalent of sodium nitrite (6.96 g, 100 mmol) was added over a period of 10 minutes while stirring with a mechanical stirrer. Stirring continued for two hours as the diazonium salt formed.

In a separate flask, 2 equivalents of ferrocene (18.64 g, 100.0 mmol) was dissolved with 50 ml of dichloromethane and 200 mL of glacial acetic acid was added. The ferrocene solution was cooled to 0 °C in an ice bath, and the diazonium solution was slowly added by using a Pasteur pipette. The reaction mixture was stirred for approximately 24 hours as it was allowed to come to room temperature. The mixture was quenched with saturated

solution of sodium bicarbonate in deionized water and the resulting solution was extracted with dichloromethane. The organic layer was collected, dried over magnesium sulfate and then filtered. Finally, the solvent is evaporated by rotary evaporator to obtain the crude product.

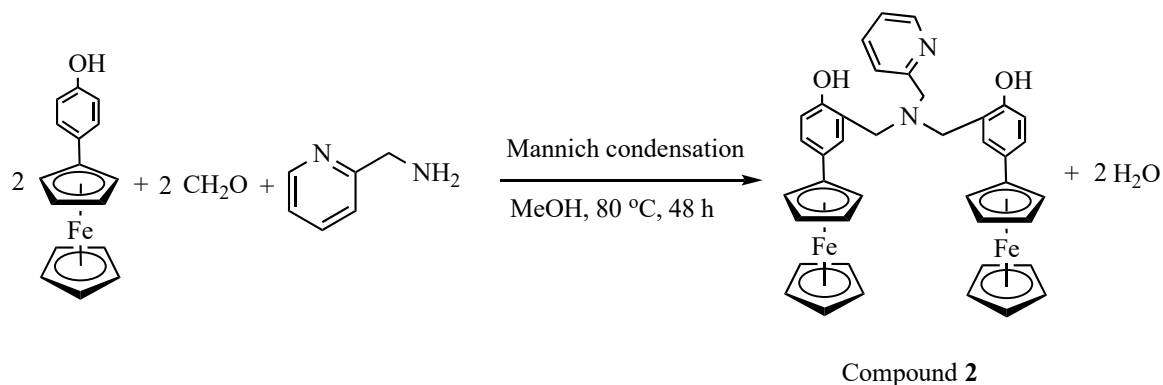


Scheme 2.1 The reactions of synthesis of compound **1**.

The 1-ferrocenyl-4-hydroxybenzene product was purified by a chromatographic column with a mobile phase of hexane-acetone (8:2 ratio). The isolated yield was 11.2% (1.56g, 5.61 mmol). Characterization for compound **1**: $^1\text{H-NMR}$ (CDCl_3 , 300 MHz, 298 K): δ 7.33 (d, $J_{\text{HH}} = 3.0$ Hz, 2H, ArH); 6.74 (d, $J_{\text{HH}} = 3.0$ Hz, 2H, ArH); 4.52 (s, 2H); 4.52 (s, 2H, FcH), 4.23 (s, 2H, FcH), 4.00 (s, 5H, FcH). $^{13}\text{C}\{^1\text{H}\}$ NMR (CDCl_3 , 75.5 MHz, 298 K): δ 153.9 (C), 127.4 (CH), 115.3 (CH), 85.9 (C), 68.5 (CH), 68.0 (C), 67.0 (CH), 66.1 (CH).

2.3 Procedure for the synthesis of a ferrocene-containing aminophenol

The reaction for synthesizing a ferrocene-containing aminophenol (called compound **2**) is shown in **Scheme 2.2**. 50 ml of methanol, 2 equivalents of compound **1** (3.00 g, 10.8 mmol) and 2 equivalents of 37 wt% formaldehyde (0.88 mL, 10.8 mmol) were added, respectively, to a 50 mL round-bottom flask equipped with a condenser. 1 equivalent of 2-picolyamine (0.58 g, 5.4 mmol) was added dropwise. Note: slow initial addition of the amine is crucial as the reaction is exothermic. The mixture was heated at reflux for 48 hours and maintained at 80 °C in an oil bath.



Scheme 2.2 The reaction of synthesis of compound **2**.

Upon cooling to room temperature, the volatiles were evaporated, and a mixture of water and dichloromethane was used for liquid-liquid extraction. Yield was 47% (1.75 g, 2.54 mmol). Characterization for compound **2**: ¹H-NMR (CDCl₃, 300 MHz, 298 K) δ 8.70 (s, 1H, PyH), 8.62 (s, 1H, PyH), 7.75 (s, 1H, PyH), 7.20 (s, 1H, PyH), 7.34 (d, J_{HH} = 6.0

Hz, 2H, ArH), 6.86 (d, $J_{\text{HH}} = 6.0$ Hz, 2H, ArH), 7.18 (s, 2H, ArH), 3.95 (s, 2H, pyCH₂N), 3.88 (s, 4H, PhCH₂N), 4.24 (s, 4H, FcH), 4.53 (s, 4H, FcH), 4.02 (s, 10H, FcH). ¹³C {¹H} NMR (CDCl₃, 75.5 MHz, 298 K): δ 156.0 (CH), 155.8 (C), 148.2 (C), 137.8 (CH), 129.8 (C), 128.1 (C), 127.5 (CH), 123.7 (CH), 122.8 (CH), 121.3 (CH), 117.2 (CH), 86.2 (C), 69.5 (CH), 68.4 (CH), 66.1 (CH), 56.5 (CH₂), 55.8 (CH₂); MS (MALDI, matrix: anthracene) m/z 686 (M-2H), 408 (M-C₁₆H₁₆FeO), 396 (M-C₁₇H₁₆FeO), 306 (M-C₂₃H₂₀FeON), 289 (M-C₂₃H₂₃FeON₂), 276 (M-C₂₄H₂₄FeON₂); Calcd for C₄₀H₃₆Fe₂N₂O₂: C, 69.77; H, 5.23; N, 4.07. Found: C, 68.75; H, 5.22; N, 5.09.

2.4 Calibration and scanning procedure for CV

The calibration procedure for the potentiostat before conducting CV scanning followed the instructions outlined in the WaveNow Wireless System User Guide, which is available on the PINE Research website.⁵⁴ At the beginning, launch the AfterMath software, which should already be installed on the computer, and log into the program. Turn on the instrument using the power switch on the back panel, then wait for the WaveNow Wireless device to appear in the list of instruments within AfterMath. The instrument's name and serial number should be visible under the "instruments" section. Review the display to check the instrument's status. Next, connect the WaveNow Wireless dummy cell (identified as Pine Research part number AB01DUM7) to the cell port located on the front panel of

the WaveNow Wireless device. Adjust the two switches on the front of the dummy cell: set switch "A" to "OFF" and switch "B" to "ON." This configuration establishes a resistive load of 49.9 k Ω . Proceed to the "AfterMath Experiments" menu and select "Cyclic Voltammetry." This action generates a "CV Parameters" node within a new archive. The expected outcome of this test is a diagonal line, and the slope of this line (approximately 20.04 μ S) corresponds to the reciprocal of the dummy cell resistance (about 49.9 k Ω). This result confirms that the instrument is ready for CV scanning and can be repeated every time during measurements.

The experiments for scanning CVs were conducted under a nitrogen atmosphere in a deoxygenated solution of dichloromethane (DCM) containing 0.1 M tetra-n-butylammonium hexafluorophosphate [nBu₄N][PF₆] at a scan rate of 100 mV/s. For the working electrode, a glassy carbon electrode (GCE, diameter: 3.0 mm) was utilized and soaked in acetone for 5-10 minutes to dissolve any organic contaminants that may have accumulated on the electrode surface. Then the electrode was rinsed with distilled water to remove any remaining acetone. Finally, the electrode was dried with Kimwipes and stored in a clean, dry place until ready to use. A Pt electrode (diameter: 6.9 mm) was used as the counter/quasi-reference electrode. To ensure accuracy and reliability, the cyclic voltammetry curves obtained from the experiments were calibrated using the

ferrocenium/ferrocene (Fc^+/Fc) redox couple as an internal standard. Prior to and after measuring the samples, the Fc^+/Fc redox couple was measured under the same experimental conditions.

Chapter 3: Results and Discussion

3.1 Characterization of compounds' structures

3.1.1 Characterization of 1-ferrocenyl-4-hydroxybenzene

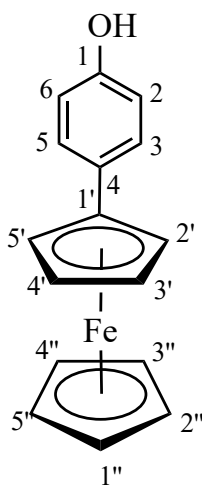


Figure 3.1 The chemical structure of compound **1**. Chemical formula: $C_{16}H_{14}FeO$, molecular weight: 278.04 g/mol, R_f value = 0.22 (hexane: acetone = 8:2), appearance: orange powder.

3.1.1.1 ¹H-NMR spectroscopy

Table 3.1 Table of ¹H-NMR signals of compound **1**.

Position	¹ H-NMR (300 MHz, CDCl ₃) δ ppm
3, 5	7.33 (d, <i>J</i> = 3.0 Hz, 2H)
2, 6	6.74 (d, <i>J</i> = 3.0 Hz, 2H)
2', 5'	4.52 (s, 2H)
3', 4'	4.23 (s, 2H)
1'', 2'', 3'', 4'', 5''	4.00 (s, 5H)

The ¹H-NMR spectrum of compound **1** is shown in **Figure 3.2** and the data summarized in **Table 3.1**. The sum of the proton integrals is equal to the number of protons in the chemical formula, which in this case is 13. The proton signals were observed in the range of 4.00 - 7.33 ppm, including 4 protons from the benzene ring and 9 protons from the ferrocenyl group.

Regarding the benzene ring, the presence of a hydroxyl group at the 4-position indicates that the ortho and para positions are more electron-rich than the meta position due

to the electron-donating nature of the hydroxyl group. Therefore, the proton signals at positions 2 and 6 (6.74 ppm) are expected to be more shielded compared to those at positions 3 and 5 (7.33 ppm). The proton at position 3 shows coupling with the proton at position 5, giving a doublet with a coupling constant of 3.0 Hz, and a similar coupling is observed between the proton at position 2 and 6.

In the ferrocenyl group, the proton signals at positions 2' and 5' have higher chemical shifts than those at positions 3' and 4' due to their proximity to the benzene ring. Additionally, the proton at position 2' is chemical equivalent to that at position 5', resulting in a singlet signal at 4.52 ppm, and a similar singlet is observed for the protons at positions 2' and 6' at 4.23 ppm. Finally, a singlet signal is observed at 4.00 ppm, indicating that all the protons at positions 1'', 2'', 3'', 4'', and 5'' are chemical equivalent.

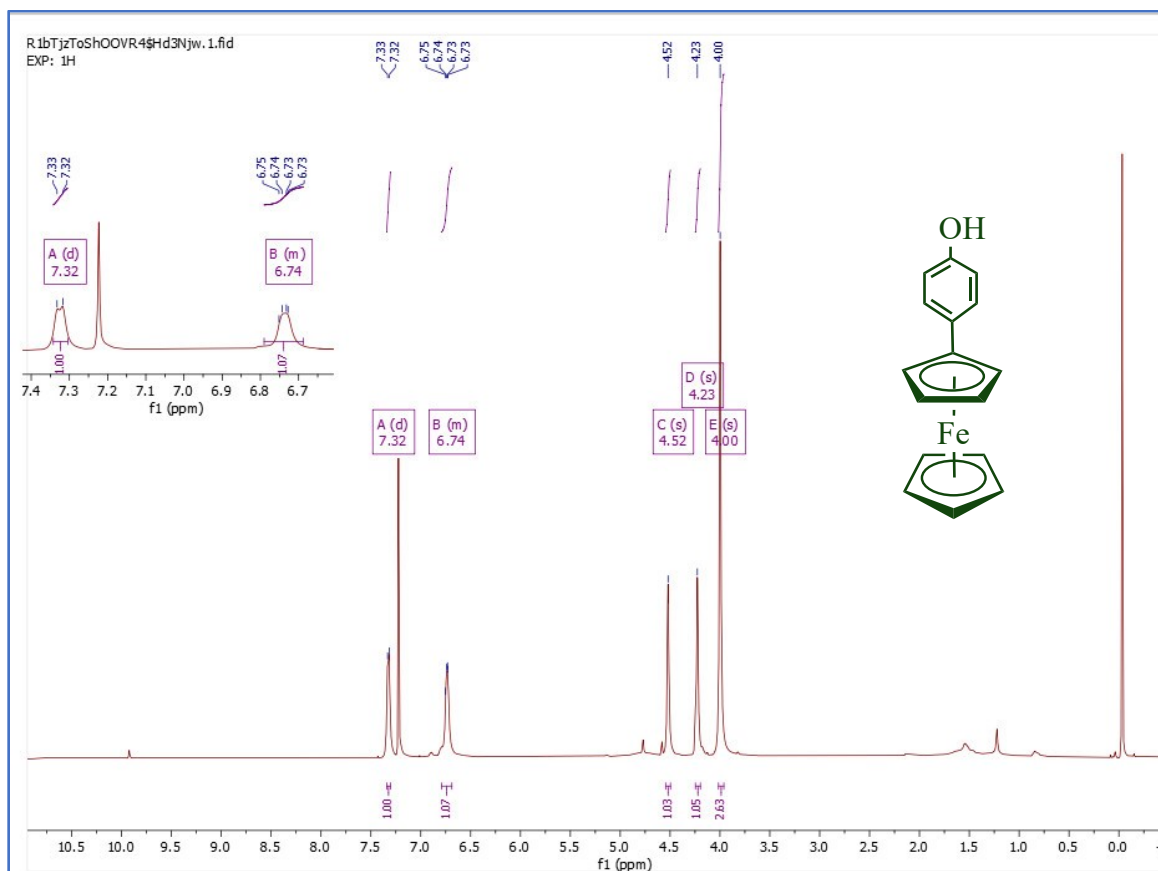


Figure 3.2 ^1H -NMR spectrum of compound **1**.

3.1.1.2 ^{13}C -NMR spectroscopy

Table 3.2 Table of ^{13}C -NMR signals of compound **1**.

Position	^{13}C -NMR (75.5 MHz, CDCl_3) δ ppm
1	153.9

4	131.5
3, 5	127.4
2, 6	115.3
1'	67.9
2', 5'	68.5
3', 4'	66.1
1'', 2'', 3'', 4'', 5''	69.5

The ^{13}C -NMR spectrum of compound **1** is presented in **Figure 3.3** and the data summarized in **Table 3.2**. The carbon signals were observed from 66.11 to 153.86 ppm. The carbons on the benzene ring are more deshielded than the carbons on the ferrocenyl group.

On the benzene ring, the electron density at the para position was higher than the position attached to the hydrogen group due to the resonance of the hydroxy group. Therefore, the chemical shift of the carbon at the 4-position (131.5 ppm) was lower than the 1-position (153.9 ppm). Besides that, the chemical shifts of carbons at positions 2 and

6 (115.3 ppm) were also lower than the carbons at positions 3 and 5 (127.4 ppm) due to the same reason.

Regarding the ferrocenyl group, the carbons gave signals at a lower field compared to the carbons of the benzene rings due to the shielding effects caused by the proximity of the ferrocenyl group to the benzene ring. The highest peak, with a chemical shift of 69.5 ppm, belonged to the five carbons of the cyclopentadienyl ring that are not attached to the benzene ring. The chemical shifts at 67.9, 68.5, and 66.1 ppm belonged to the carbons of the cyclopentadienyl ring attached to the benzene ring.

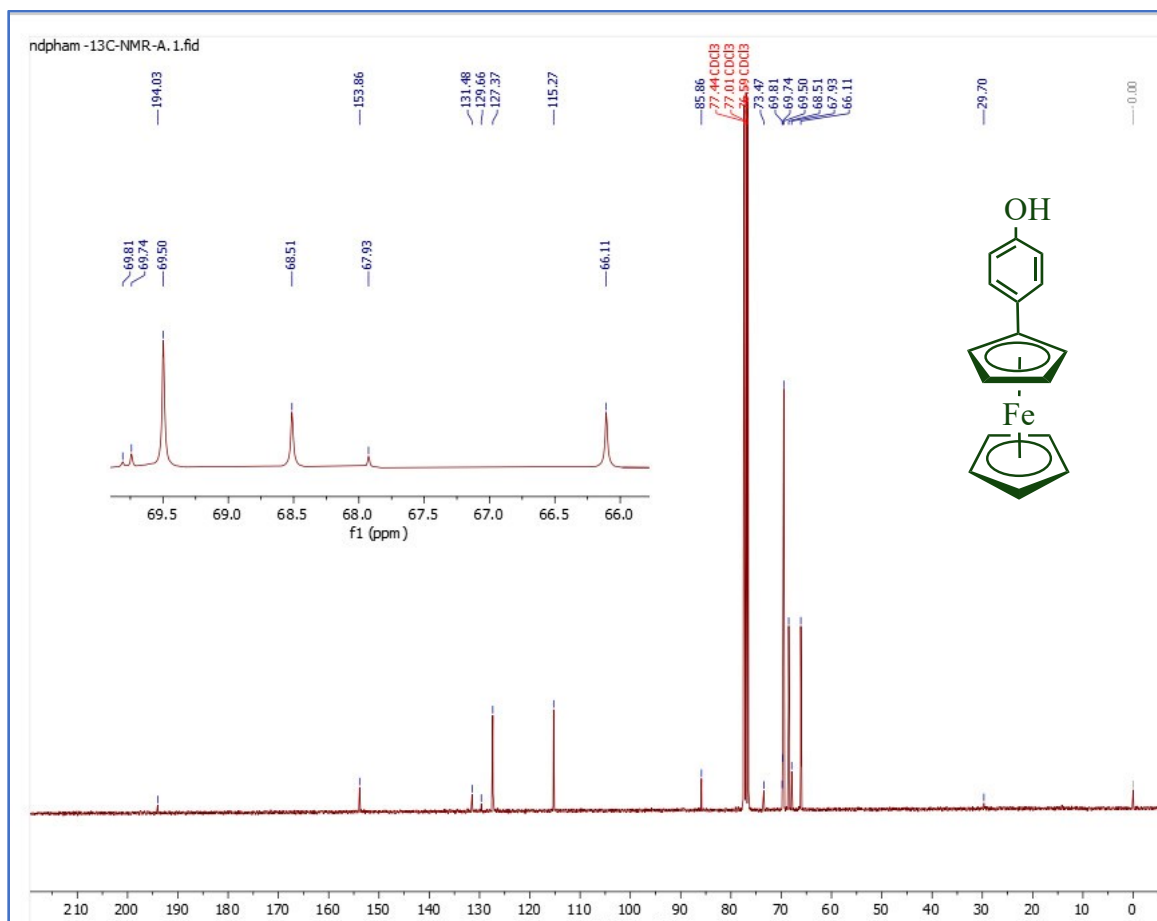


Figure 3.3 ^{13}C -NMR spectrum of compound **1**.

3.1.2 Characterization of a ferrocene-containing aminophenol

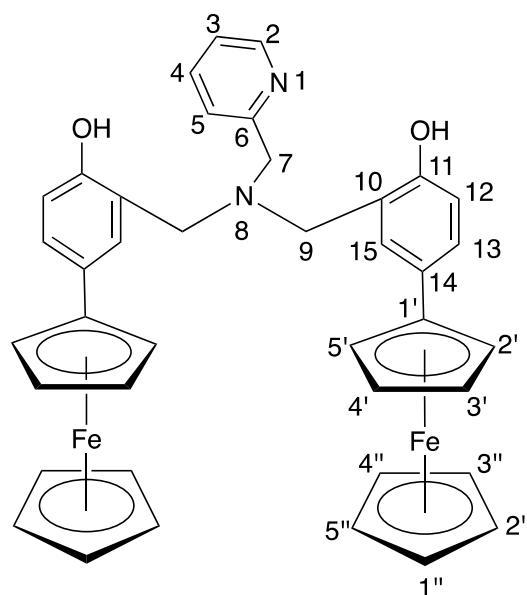


Figure 3.4 The chemical structure of compound **2**. Chemical formula: $C_{40}H_{36}Fe_2N_2O_2$, molecular weight: 688.14 g/mol, melting point: 170-171 °C, appearance: yellow powder.

3.1.2.1 1H -NMR spectroscopy

Table 3.3 Table of 1H -NMR signals of compound **2**.

Position	1H -NMR (300 MHz, $CDCl_3$) δ ppm
2	8.70 (s, 1H)
3	8.62 (s, 1H)

4	7.75 (s, 1H)
5	7.20 (s, 1H)
12	7.34 (d, $J = 6.0$ Hz, 2H)
13	6.86 (d, $J = 6.0$ Hz, 2H)
15	7.18 (s, 2H)
7	3.95 (s, 2H)
9	3.88 (s, 4H)
3', 4'	4.24 (s, 4H)
2', 5'	4.53 (s, 4H)
1'', 2'', 3'', 4'', 5''	4.02 (s, 10H)

The ^1H -NMR spectrum of compound **2** is presented in **Figure 3.5** and the data summarized in **Table 3.3**. The 2 protons at positions 12 and 13 are coupled to each other, resulting in 2 doublet signals, and they have a coupling constant of 6 Hz.

The proton signals at positions 2' and 5' in the ferrocenyl group exhibit higher chemical shifts compared to positions 3' and 4' due to their proximity to the benzene ring. The proton at position 2' is chemical equivalent to the one at position 5', resulting in a singlet signal at 4.53 ppm. Similarly, the protons at positions 3' and 4' are also symmetrical, producing a singlet signal at 4.24 ppm. Lastly, the singlet peak at 4.03 ppm includes the symmetry of all the protons at positions 1'', 2'', 3'', 4'', and 5''.

In the ^1H -NMR spectrum, the proton signals detected at positions 2, 3, 4, and 5 can be attributed to the pyridine group. These specific positions on the spectrum indicate the presence of protons associated with the pyridine moiety.

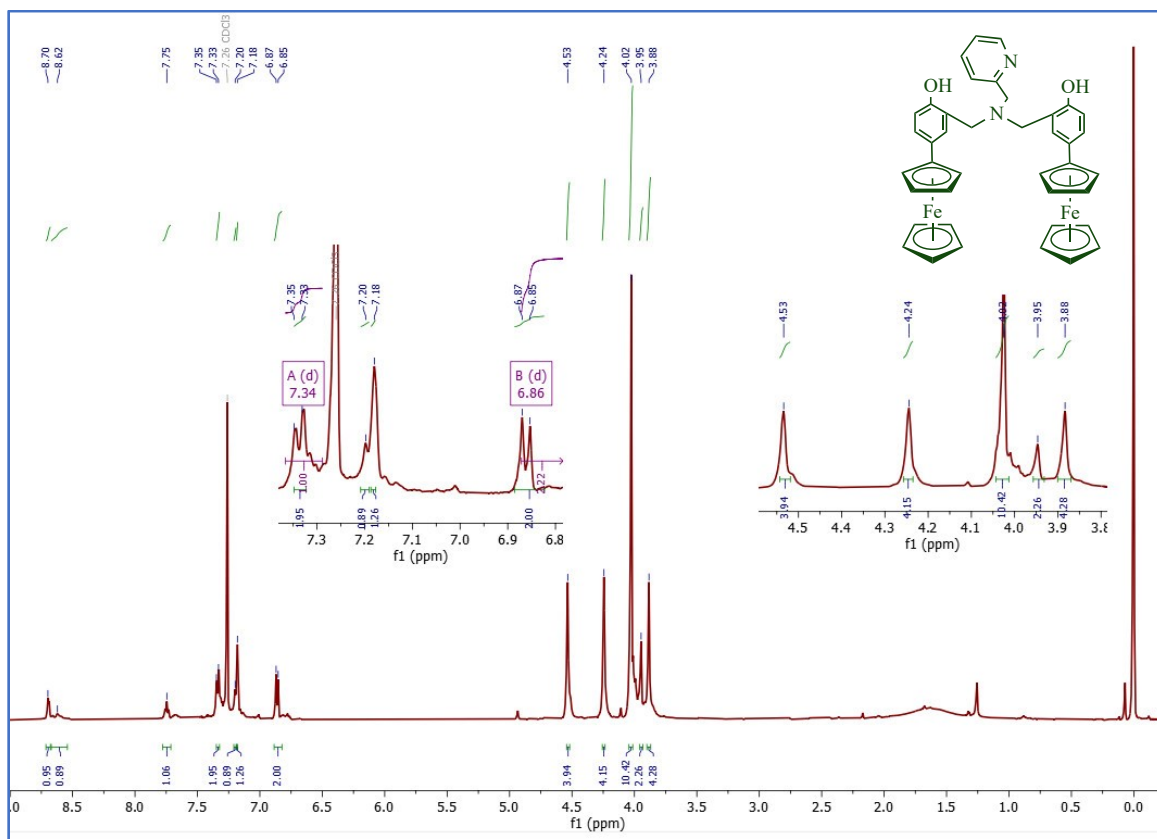


Figure 3.5 $^1\text{H-NMR}$ spectrum of compound 2.

3.1.2.2 $^{13}\text{C-NMR}$ spectroscopy

Table 3.4 Table of $^{13}\text{C-NMR}$ signals of compound 2.

Position	$^{13}\text{C-NMR}$ (75.5 MHz, CDCl_3) δppm
11	156.0
2	155.8

6	148.2
3	137.8
10	129.8
14	128.1
12	127.5
4	123.7
5	122.8
15	121.3
13	117.2
1'	86.2
1'', 2'', 3'', 4'', 5''	69.5
3'	68.4
2'	66.1

9	56.5
7	55.8

The ^{13}C -NMR spectrum of compound **2** is presented in **Figure 3.6** and the data summarized in **Table 3.4**. According to the ^{13}C -NMR result of compound **2**, it can be seen that there are 17 signals of carbon which are suitable for the structure of this compound. Signals are observed in the downfield region more than 120 ppm belonging to carbons of aromatic rings. While those in upfield region less than 120 ppm are signals corresponding to sp^3 -carbons and those of ferrocene. For example, there are several more shielded protons whose peaks are at region of 60 - 90 ppm which can be assigned as signals of the ferrocenyl groups.

Looking more closely to the region more deshielded than 120 ppm, it is evident that the intensity of the signal for the carbons of the pyridine ring are weaker than carbon signals for the benzene ring. This is because there are two benzene rings which chemical equivalent in the structure of compound **2**. In addition, carbons which are closer to a nitrogen atom generally are more deshielded such as the carbon

at position 2 (155.8 ppm) and 6 (148.2 ppm). This is explained by the nitrogen atom being relatively electronegative, which deshields the nearby carbons and causes them to experience a stronger magnetic field.

In many ways, the explanation used for compound **1**'s spectrum can be used for compound **2**. The electron-donating effect of hydroxy group on benzene ring in compound **2** means carbons at ortho and para positions are observed in downfield region.

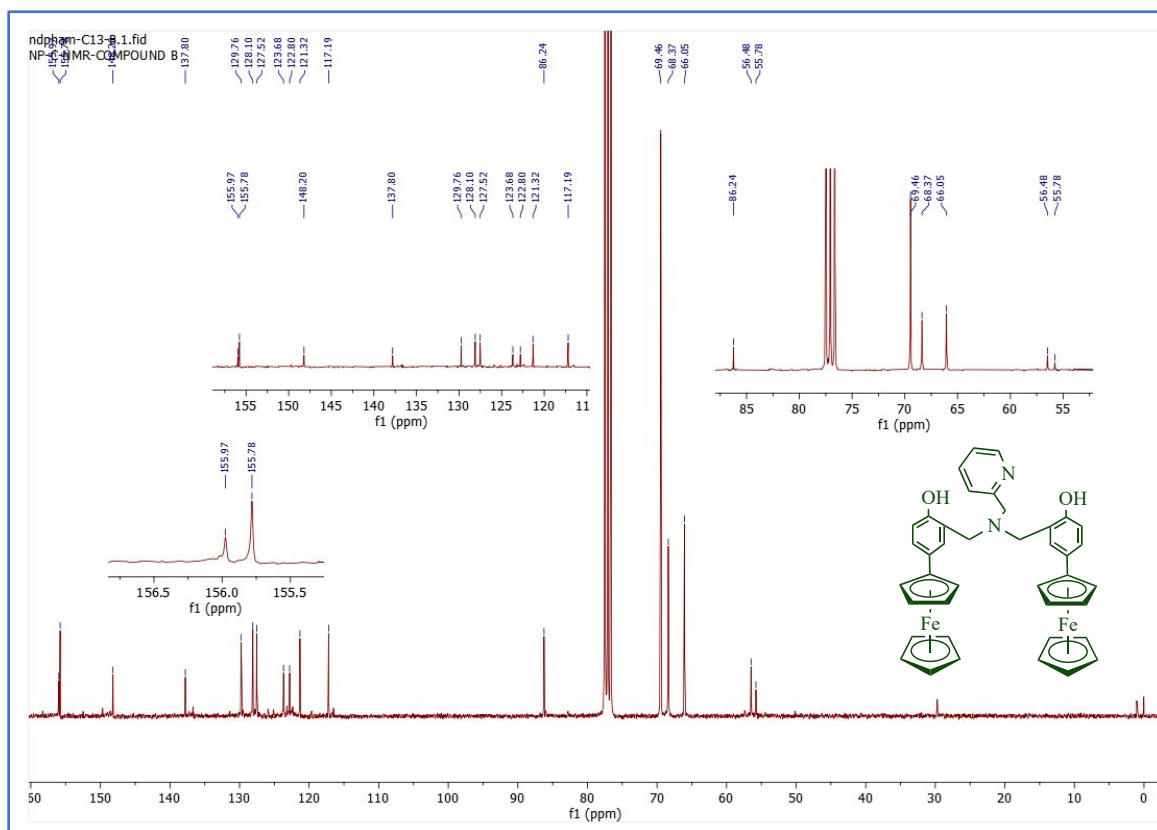


Figure 3.6 ^{13}C -NMR spectrum of compound **2**.

3.1.2.3 MALDI-TOF mass spectrometry

Matrix-assisted laser desorption/ionization time-of-flight mass spectrometry (MALDI-TOF MS) was first introduced in 1987⁵⁵ and originally developed for non-volatile and large biomolecules.^{55,56} MALDI-TOF MS has advantages over other methodologies, including speed of analysis, high sensitivity, wide applicability combined with a good tolerance toward contaminants, and the ability to analyze complex mixtures.^{57,58} However, for the compounds of interest, the selection of a proper matrix in combination with various methods of sample preparation is very important. In addition, good signal-to-noise ratios and spot-to-spot repeatability are essential to acquiring a good MALDI-TOF MS spectrum for data analysis. In this thesis, compound **2** could be readily dissolved in dichloromethane, CH₂Cl₂, and were thus combined with anthracene (also soluble) as a matrix in a 1:1 ratio.

Anthracene is a small organic molecule consisting of three fused benzene rings, and an ideal matrix for this ligand due largely in part to its lack of functional groups; it generates radical cations for the molecular ion of the ligand through electron abstraction (**Figure 3.7**).⁵⁹

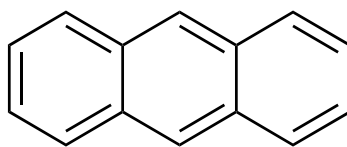


Figure 3.7 The structure of anthracene.

Anthracene is widely used as a matrix compound in MALDI-TOF MS due to its advantageous properties. It efficiently absorbs laser energy, facilitating the ionization of analyte molecules and the generation of gas-phase ions. Additionally, anthracene exhibits low background noise in mass spectra, enabling clear detection of analyte ions. Anthracene also enhances the signal intensity of certain analytes, resulting in improved sensitivity during analysis. Moreover, it demonstrates stability and resilience under the experimental conditions of MALDI-TOF MS, making it a reliable matrix compound choice.^{60,61}

In MALDI-TOF MS, a sample is mixed with a matrix compound and spotted onto a metal plate. The matrix absorbs the laser energy and transfers it to the sample, causing it to ionize and form gas-phase ions. These ions are then accelerated by an electric field and travel through a flight tube, where they are separated based on their mass-to-charge ratio (m/z). Finally, the ions are detected and recorded by a detector, producing a mass spectrum.⁶²

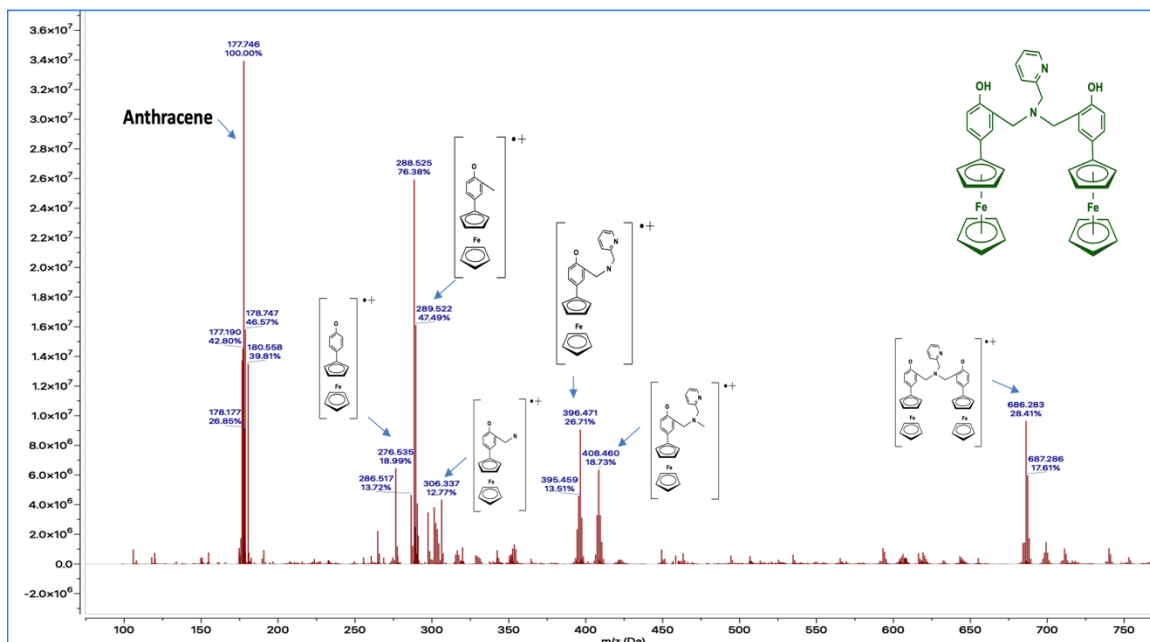


Figure 3.8 MALDI-TOF MS spectrum of compound **2** dissolved in dichloromethane, CH_2Cl_2 and were thus combined with anthracene (also soluble) as a matrix in a 1:1 ratio at the positive mode.

The positive ion spectra of compound **2** ($\text{C}_{40}\text{H}_{36}\text{Fe}_2\text{O}_2\text{N}_2$, $M = 688.14$) can be observed in **Figure 3.8** using MALDI-TOF MS. Within this figure, the fragments encompassing mass-to-charge ratios (m/z) ranging from 276 to 687 are presented. These fragments are indicated below, and their values are measured in Daltons (Da).

$$m/z = 686.283 = [\text{M} - 2\text{H}]^{\bullet+} = [\text{C}_{40}\text{H}_{34}\text{Fe}_2\text{O}_2\text{N}_2]^{\bullet+}$$

$$m/z = 408.46 = [\text{C}_{40}\text{H}_{34}\text{Fe}_2\text{O}_2\text{N}_2 - \text{C}_{16}\text{H}_{14}\text{FeO}]^{\bullet+} = [\text{C}_{24}\text{H}_{20}\text{FeON}_2]^{\bullet+}$$

$$m/z = 396.471 = [\text{C}_{24}\text{H}_{20}\text{FeON}_2 - \text{C}]^{\bullet+} = [\text{C}_{23}\text{H}_{20}\text{FeON}_2]^{\bullet+}$$

$$m/z = 306.337 = [\text{C}_{23}\text{H}_{20}\text{FeON}_2 - \text{C}_6\text{H}_4\text{N}]^{\bullet+} = [\text{C}_{17}\text{H}_{16}\text{FeON}]^{\bullet+}$$

$$m/z = 289.522 = [\text{C}_{17}\text{H}_{16}\text{FeON} - \text{NH}_3]^{\bullet+} = [\text{C}_{17}\text{H}_{13}\text{FeO}]^{\bullet+}$$

$$m/z = 276.535 = [\text{C}_{17}\text{H}_{13}\text{FeO} - \text{CH}]^{\bullet+} = [\text{C}_{16}\text{H}_{12}\text{FeO}]^{\bullet+}$$

Fragmentation in the MALDI-TOF MS analysis of compound **2** provides insights into its molecular weight, molecular formula, and potential structure characteristics.

3.1.2.4 X-ray crystallography

Scientists use X-ray crystallography to study the structure of crystals and molecules. This method involves directing X-rays onto a crystal and measuring the resulting diffraction pattern, revealing information about the atoms' arrangement within the crystal or molecule. X-ray crystallography has played a pivotal role in advancing many scientific disciplines, including biology, chemistry, materials science, and physics.⁶³ In recognition of its importance, the United Nations General Assembly designated 2014 as the International Year of Crystallography⁶⁴ to raise awareness about its contributions to scientific research and promote international cooperation in this field. Single-crystal X-ray diffraction is a reliable technique for determining the three-dimensional structure of small organic molecules. It provides detailed information about bond lengths, bond angles, and molecular conformations, which are essential for understanding the properties and behaviour of the molecule.

Orange crystals of compound **2** of suitable size and quality for X-ray diffraction analysis were grown by slow evaporation of a solution of the complex in a mixture of dichloromethane and methanol at room temperature. The resulting crystals were isolated, and the structures of compound **2** was determined by X-ray diffraction analysis. The structure of the ferrocene-containing amino phenol showed two ferrocenyl groups, two phenol groups, and one central amine group and a pyridine group as shown in **Figure 3.9**.

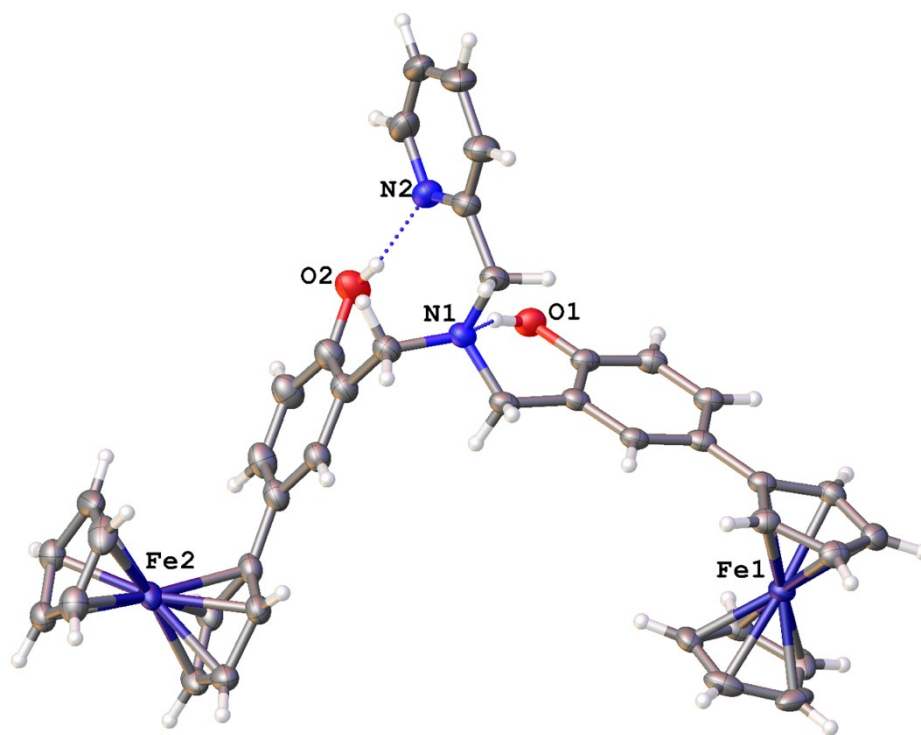


Figure 3.9 X-ray crystal structure of compound **2** (Non-hydrogen atoms are represented by displacement ellipsoids at the 30% probability level).

The compound **2** is crystallized as a monoclinic crystal system. In crystallography, the term "crystal system" refers to seven categories that classify crystals based on their symmetry and the shape of their unit cell. These seven crystal systems are cubic, tetragonal, orthorhombic, rhombohedral, hexagonal, triclinic, and monoclinic.⁶³ Monoclinic is one of the seven crystal systems, and it describes crystals with a unit cell that has three unequal axes, two of which intersect at an oblique angle (i.e., not a right angle). This means that the crystal has a unique axis of symmetry, which is different from the other crystal systems with higher degrees of symmetry. The crystal has three distinct lattice parameters: $a = 21.0806 \text{ \AA}$, $b = 6.04370 \text{ \AA}$, and $c = 26.0952 \text{ \AA}$, while the angle between the b and c axes is 101.510° (**Table 3.5**). The numbers in parentheses denote the estimated standard deviations in the final digit(s) of each value, reflecting the measurement's precision. When the value of Z is given as 4, it means that there are 4 molecules in the unit cell of the crystal structure being described. This value is important because it provides information about the density, composition, and other properties of the crystal.

In X-ray crystallography, the term "R indices" refer to the agreement between the observed diffraction data and the calculated structure factors. These indices provide a measure of how well the model fits the experimental data. The final R indices [$I \geq 2\sigma(I)$] is a commonly reported value that indicates the agreement between the measured intensities

of the reflections (I) and the calculated intensities (I) based on the atomic model. The value of " $I \geq 2\sigma(I)$ " means that only the intensities of reflections that are at least two standard deviations above the noise level are included in the calculation of the R indices. This helps to ensure that the calculated R value is reliable and not significantly affected by measurement errors or other sources of noise.^{65,66} The final R indices [$I \geq 2\sigma(I)$] is a critical metric used to assess the quality of a crystallographic model. Lower values of R indices indicate a better agreement between the observed and calculated data and therefore a higher quality model. This value is typically reported along with other crystallographic statistics, such as the resolution of the data and the number of reflections used in the refinement. Based on the obtained R1 value of 0.0543 and wR2 value of 0.1480 for compound **2**, the data meets the criteria for good quality and acceptability. In many scientific fields, R1 values of less than 0.10 and wR2 values of less than 0.20 are generally considered acceptable as a good resolution.^{66,67}

Table 3.5 Crystal data and structure refinement of compound **2**

Identification code	NP3001 (compound 2)
Empirical formula	C ₄₂ H ₄₂ Fe ₂ N ₂ O ₃ (C ₄₀ H ₃₆ Fe ₂ N ₂ O ₂ .C ₂ H ₆ O)
Formula weight	734.47

Temperature/K	100(2)
Crystal system	monoclinic
Space group	$P2_1/n$
$a/\text{\AA}$	21.0806(3)
$b/\text{\AA}$	6.04370(10)
$c/\text{\AA}$	26.0952(4)
$\beta/^\circ$	101.510(2)
Volume/ \AA^3	3257.79(9)
Z	4
$\rho_{\text{calc}}/\text{g/cm}^3$	1.497
μ/mm^{-1}	7.497
$F(000)$	1536.0
Crystal size/ mm^3	$0.143 \times 0.064 \times 0.039$
Radiation	Cu $K\alpha$ ($\lambda = 1.54184$)
2θ range for data collection/ $^\circ$	4.934 to 158.688
Index ranges	$-26 \leq h \leq 26, -7 \leq k \leq 7, -33 \leq l \leq 32$
Reflections collected	35443
Independent reflections	6975 [$R_{\text{int}} = 0.0592, R_{\text{sigma}} = 0.0398$]
Data/restraints/parameters	6975/66/470
Goodness-of-fit on F^2	1.032
Final R indexes [$I \geq 2\sigma(I)$]	$R_1 = 0.0543, wR_2 = 0.1480$
Final R indexes [all data]	$R_1 = 0.0737, wR_2 = 0.1643$
Largest diff. peak/hole / $e \text{\AA}^{-3}$	1.19/-0.37

Hydrogen bonding between nitrogen (N) and hydrogen (H), as well as Van der Waals bonding between oxygen (O) and nitrogen (N), can play a crucial role in stabilizing

crystal structures (**Table 3.6**). Nitrogen-containing groups, such as amides, imines, and amines, are frequently involved in hydrogen bonding interactions that lead to the formation of extended networks of hydrogen-bonded molecules within the crystal lattice. Similarly, the electronegativity difference between O and N creates a polarized molecule that can interact weakly through Van der Waals forces. These networks provide additional stability to the crystal structure and also affect its properties, such as solubility, melting point, and reactivity.

Table 3.6 Calculation of the hydrogen bonding among 3 elements: O, H, N (Van der Waals radii of Nitrogen (N)=1.55 Å, Hydrogen (H) = 1.20 Å, Oxygen (O) = 1.52 Å).

D	H	A	d(D-H)/Å	d(H-A)/Å	d(D-A)/Å
O1	H1	N1	0.89(2)	1.85(3)	2.663(4)
Sum of Van der Waals radii			-	2.75 > 1.85	3.070 > 2.663
Conclusions			O1 and H1 form a hydroxyl group	an interaction (hydrogen bonding between N1 and H1)	an interaction (Van der Waals bonding between O1 and N1)

O2	H2	N2	0.86(2)	1.90(3)	2.738(5)
Sum of Van der Waals radii			-	2.75 > 1.90	3.070 > 2.738
Conclusions			O2 and H2 form a hydroxyl group	an interaction (hydrogen bonding between N2 and H2)	an interaction (Van der Waals bonding between O2 and N2)

3.1.2.5 UV-Vis spectroscopy

A representative set of UV-Vis spectrum for ferrocene, compound **1** and compound **2** showcase the effect of installing different functional groups onto ferrocene. They exhibit intense bands in both the ultraviolet (UV) and visible regions. As shown in **Figure 3.10**, the maximum peak in UV region is at approximately 320 nm and 340 nm, which can be attributed to the intense $n \rightarrow \pi^*$ transition from the phenolic rings and pyridine group in compound **2**, respectively. The lone pair of electrons on the oxygen atom of the hydroxyl group contributes to the delocalized electron cloud, making the phenolic ring highly conjugated and susceptible to UV-Vis absorption. This characteristic is evident in compound **1** and compound **2**. Moreover, when exposed to UV or visible light, the pyridine

group can undergo electronic transitions between these molecular orbitals. The $n \rightarrow \pi^*$ transition specifically refers to the excitation of an electron from the nitrogen lone pair (n orbital) to an antibonding π^* orbital within the π electron cloud. The energy required for the $n \rightarrow \pi^*$ transition typically falls within the UV or higher-energy visible light region. Thus, compound **2** exhibits two maximum peaks in the UV region at ~ 320 nm and ~ 340 nm, associated with the transition of the phenolic and pyridine rings, respectively.

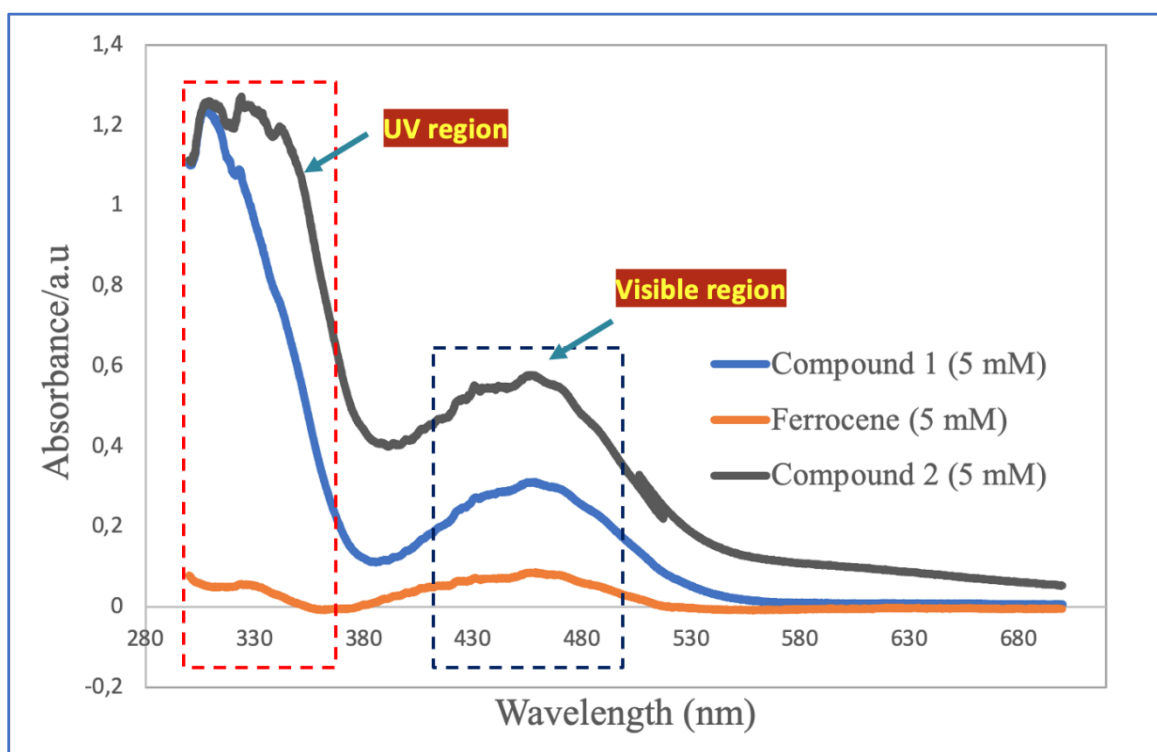


Figure 3.10 The comparison UV-Vis spectrum of ferrocene, compound **1**, and compound **2**, diluted in dichloromethane (DCM) at the concentration of 5 mM (room temperature).

In the visible region, according to the Beer-Lambert law, the equation is: $A = \epsilon CL$, where A represents Absorbance, ϵ is the molar absorption coefficient ($M^{-1}cm^{-1}$), C is the molar concentration (M), and L is the optical path length (cm). Therefore, the molar absorption coefficient of prepared compounds was calculated follows:

$$\epsilon_{\text{ferrocene}} = 17.0 M^{-1}cm^{-1} \text{ at } \lambda_{\text{max}} = 456 \text{ nm}$$

$$\epsilon_{\text{compound 1}} = 62.0 M^{-1}cm^{-1} \text{ at } \lambda_{\text{max}} = 457 \text{ nm}$$

$$\epsilon_{\text{compound 2}} = 115 M^{-1}cm^{-1} \text{ at } \lambda_{\text{max}} = 455 \text{ nm}$$

Absorbances in the UV-Vis spectra in the visible region were observed for compound **1** and compound **2** at almost the same wavelength as ferrocene (456 nm). However, compound **1** has one ferrocenyl group and one phenol group, while compound **2** has two ferrocenyl groups combine with two phenol groups. As a result, compound **2** exhibits the highest molar absorption coefficient among them, while compound **1** also displays a higher molar absorption coefficient than ferrocene. Thus, the molar absorption coefficient of compound **2** > the molar absorption coefficient of compound **1** > the molar absorption coefficient of ferrocene ($\epsilon_{\text{compound 2}} > \epsilon_{\text{compound 1}} > \epsilon_{\text{ferrocene}}$).

3.2 Electrochemical behaviour of compounds

3.2.1 Cyclic voltammetry (CV)

Cyclic voltammetry (CV) is a versatile and widely used electroanalytical technique that has proved invaluable in the study of electroactive species. This technique has found broad application in the fields of electrochemistry, inorganic chemistry, organic chemistry, and biochemistry, due to its ease of measurement and versatility. CV is often the first experiment and typically displays a characteristic shape performed when investigating a compound, a biological material, or an electrode surface because it allows for the rapid observation of redox behavior over a wide potential range. The anodic peak corresponds to the oxidation of the electroactive species, while the cathodic peak corresponds to its reduction. The potential at which the anodic peak occurs is known as the oxidation potential, and the potential at which the cathodic peak occurs is known as the reduction potential. The separation between the two peaks, known as the peak-to-peak separation, is a measure of the reversibility of the electrochemical reaction.⁶⁸⁻⁷⁰

Moreover, CVs can provide valuable information about the redox properties of a sample, such as the number of electrons involved in the reaction, the stability of the intermediates, and the kinetics of the reaction. CVs can also be used to study the adsorption of species onto electrode surfaces and to determine the surface area of electrodes. The

resulting voltammogram, which is obtained by plotting the current response against the applied potential, is analogous to a conventional spectrum in that it conveys information as a function of an energy scan.^{68,71}

3.2.2 Electrochemical behaviour of ferrocene

The CV curve of ferrocene is shown in **Figure 3.11**. The half-wave potential of the ferrocenium/ferrocene (Fc^+/Fc) redox couple ($E_{1/2, \text{Fc}^+/\text{Fc}}$) was estimated from $E_{1/2, \text{Fc}^+/\text{Fc}} = (E_{\text{ox}} + E_{\text{red}})/2$, where E_{ox} and E_{red} are the oxidation and reduction peak potentials, respectively. The half-wave potential of Fc^+/Fc was found to be 49.6 mV (**Table 3.7**) $\{E_{1/2, \text{Fc}^+/\text{Fc}} = (E_{\text{ox}} + E_{\text{red}})/2 = (11.5 + 87.7)/2 = 49.6 \text{ mV}\}$ related to the Fc^+/Fc external standard reference electrode. This allows other data to be corrected relative to this external Fc^+/Fc standard ($\text{Fc}^+/\text{Fc} = 0 \text{ mV}$).

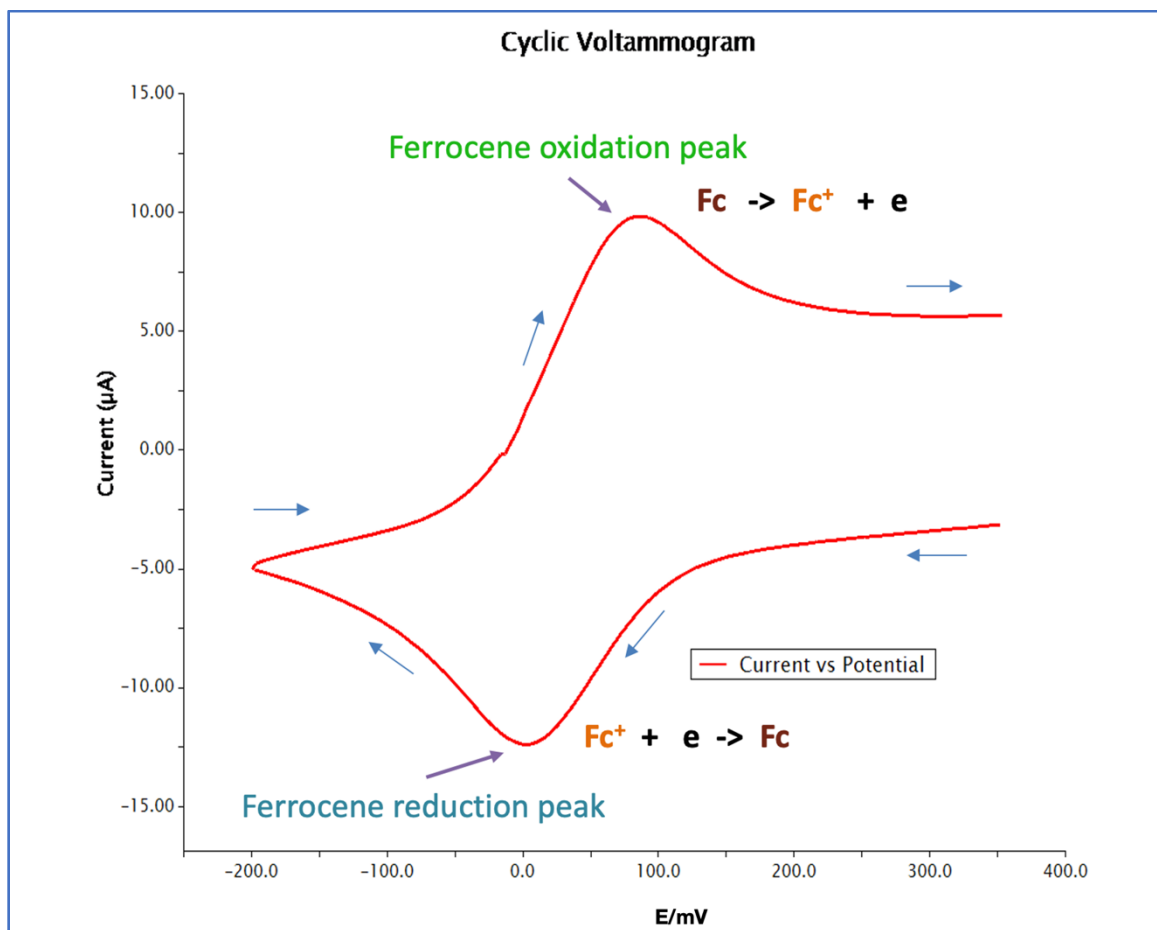


Figure 3.11 The cyclic voltammogram of ferrocene (5 mM) was recorded in dichloromethane (DCM) of solution of tetra-n-butylammonium hexafluorophosphate [Bu_4N][PF_6] (0.1 M). Scan rate: 100 mV/s.

Table 3.7 The calculation of half-wave potential of ferrocene.

The calculation of half-wave potential of ferrocene		
	Current (μA)	Potential (mV)
Reduction peak	9.84	87,7
Oxidation peak	-12,2	11,5
Half-wave potential	-1,20	49,6

3.2.3 Electrochemical behaviour of 1-ferrocenyl-4-hydroxybenzene

The redox behaviour of ligands and complexes is greatly influenced by various conditions, such as the choice of solvent, the type of electrode employed, and the composition of the electrolyte. In order to assess the redox properties of compound **1**, it was subjected to investigation through cyclic voltammetry under identical conditions as those utilized for the analysis of ferrocene. A cyclic voltammogram of compound **1** in dichloromethane (DCM) at a scan rate of 100 mV/s is presented in **Figure 3.12**. The obtained voltammogram serves as a graphical representation of the redox behaviour of compound **1**, illustrating the oxidation and reduction peaks observed at different potentials during the scan. Through this analysis, the electrochemical properties of compound **1** can be further elucidated, facilitating a better understanding of its overall reactivity.

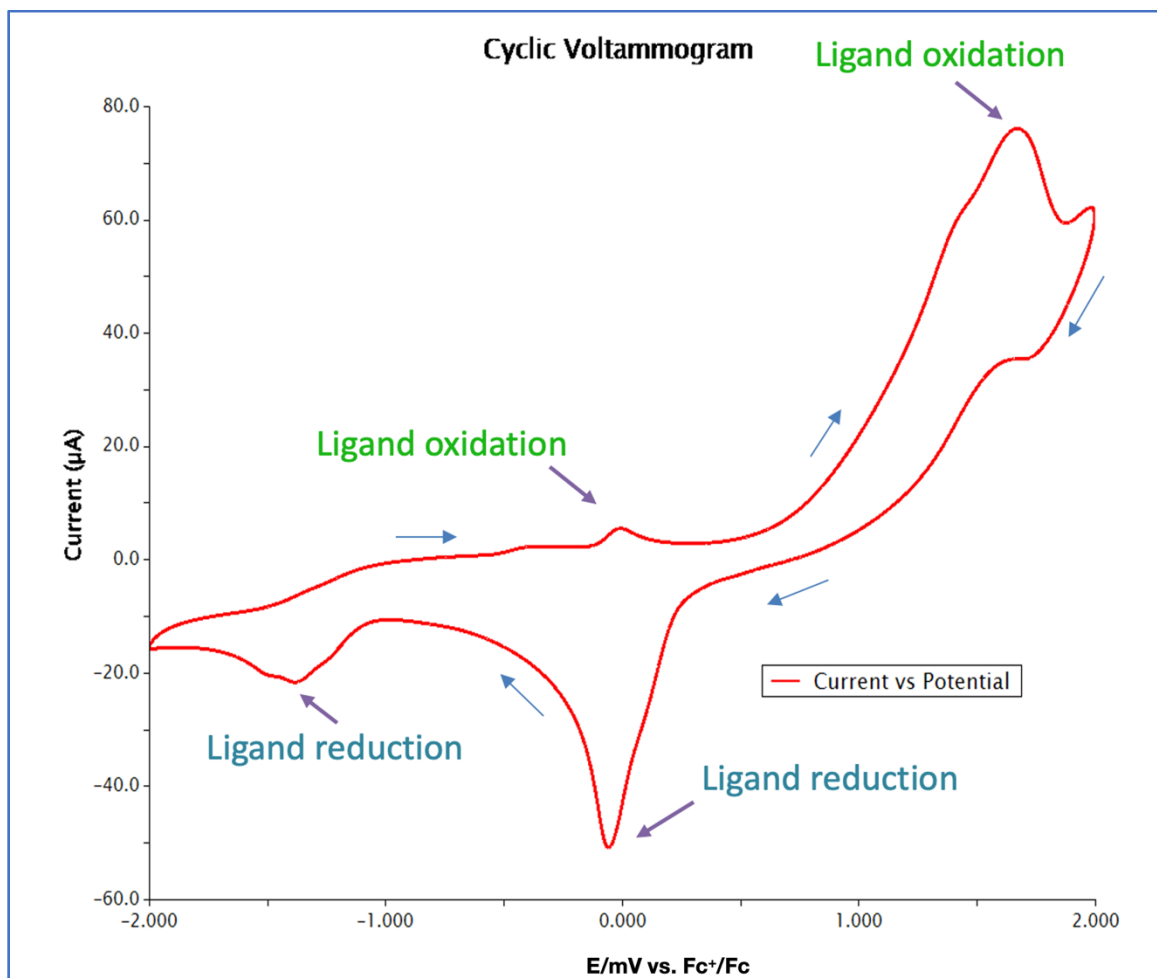


Figure 3.12 The cyclic voltammogram of compound **1** (5 mM) was recorded in dichloromethane (DCM) of solution of tetra-n-butylammonium hexafluorophosphate [ⁿBu₄N][PF₆] (0.1 M). Scan rate: 100 mV/s. Potential versus Fc⁺/Fc.

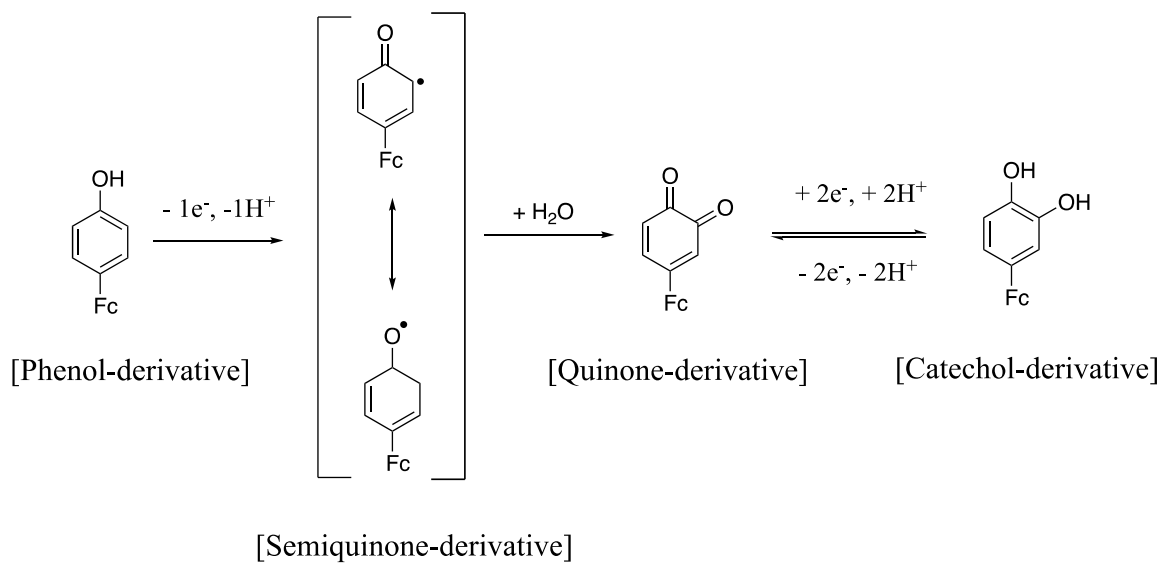
The CV of the compound **1** display a very weakly quasi-reversible oxidation. They showed very strong reduction peak at 0.0579 mV. The half-wave potential of compound **1** was found to be -0.0345 mV (**Table 3.8**) $\{E_{1/2, Fc^+/Fc} = (E_{ox} + E_{red})/2 = (-0.0111 + -0.0579)/2 = -0.0345 \text{ mV}\}$ versus Fc⁺/Fc.

Table 3.8 The calculation of half-wave potential of compound **1** versus Fc^+/Fc .

The calculation of half-wave potential of compound 1 versus Fc^+/Fc		
	Current (μA)	Potential (mV)
Reduction peak	-50.8	-0.0579
Oxidation peak	5.57	-0.0111
Half-wave potential	-22.6	-0.0345

The mechanism of electrochemical oxidation and reduction of compound **1** was investigated through cyclic voltammetry. Under the experimental conditions, compound **1** exhibited an oxidation process characterized by a single-step peak at $E_{\text{ox}} = +1.70$ V. This oxidation mechanism involves the transfer of one electron and one proton from a phenol-derivative to a quinone-derivative. While scanning negatively, a second distinct reduction peak was observed at $E_{\text{red}} = -1.40$ V. This cathodic peak corresponds to the reduction of the quinone-derivative (two phenol oxidation products) to a catechol-derivative, and it involves the transfer and acceptance of two electrons and two protons, as illustrated in **Scheme 3.1**.⁷² Cyclic voltammetry provides valuable information about the electrochemical behaviour of compounds. Thus, the oxidation peak observed at +1.70 V suggests the presence of an oxidation process involving the conversion of the phenol-derivative to the quinone-

derivative. Similarly, the reduction peak at -1.40 V indicates the reduction of the quinone-derivative to the catechol-derivative.



Scheme 3.1 Proposed mechanism for electrochemical oxidation of compound **1** via cyclic voltammetry.

3.2.4 Electrochemical behaviour of a ferrocene-containing aminophenol

The electrochemical behaviour of compound **2** was measured under the same conditions as compound **1**. A complete cyclic voltammogram of compound **2** in dichloromethane at a scan rate of 100 mV/s is shown in **Figure 3.13**. Similar to compound **1**, the CV of the compound **2** displays a very weakly quasi-reversible oxidation. It showed a very strong reduction peak 0.0278 mV and weak oxidation peak at 0.0314 mV at the position of Fc⁺/Fc couple. The half-wave potential of compound **2** was found to be 0.0296 mV (**Table 3.9**) $\{E_{1/2, \text{Fc}^+/\text{Fc}} = (E_{\text{ox}} + E_{\text{red}})/2 = (0.0278 + 0.0314)/2 = 0.0296 \text{ mV}\}$ versus Fc⁺/Fc.

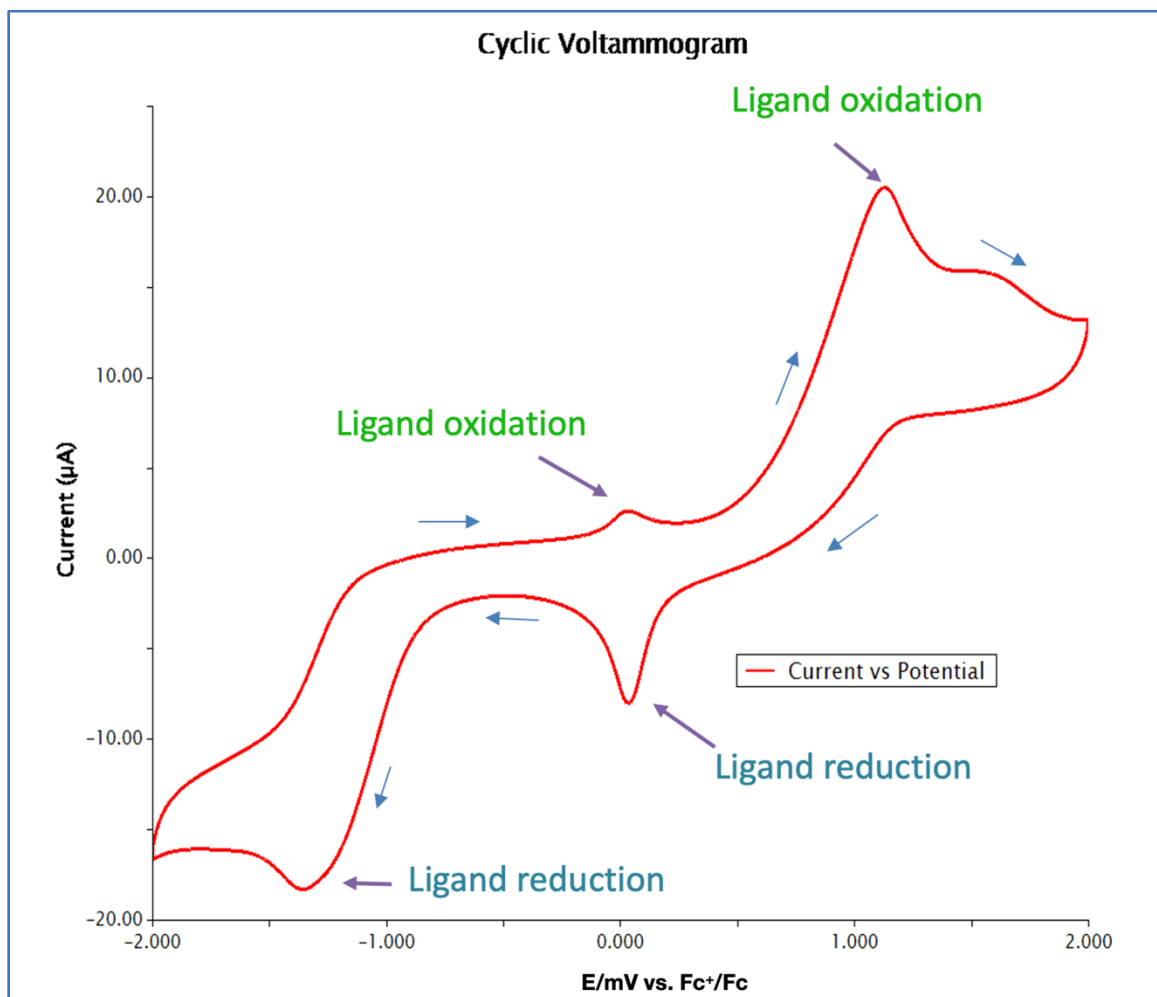


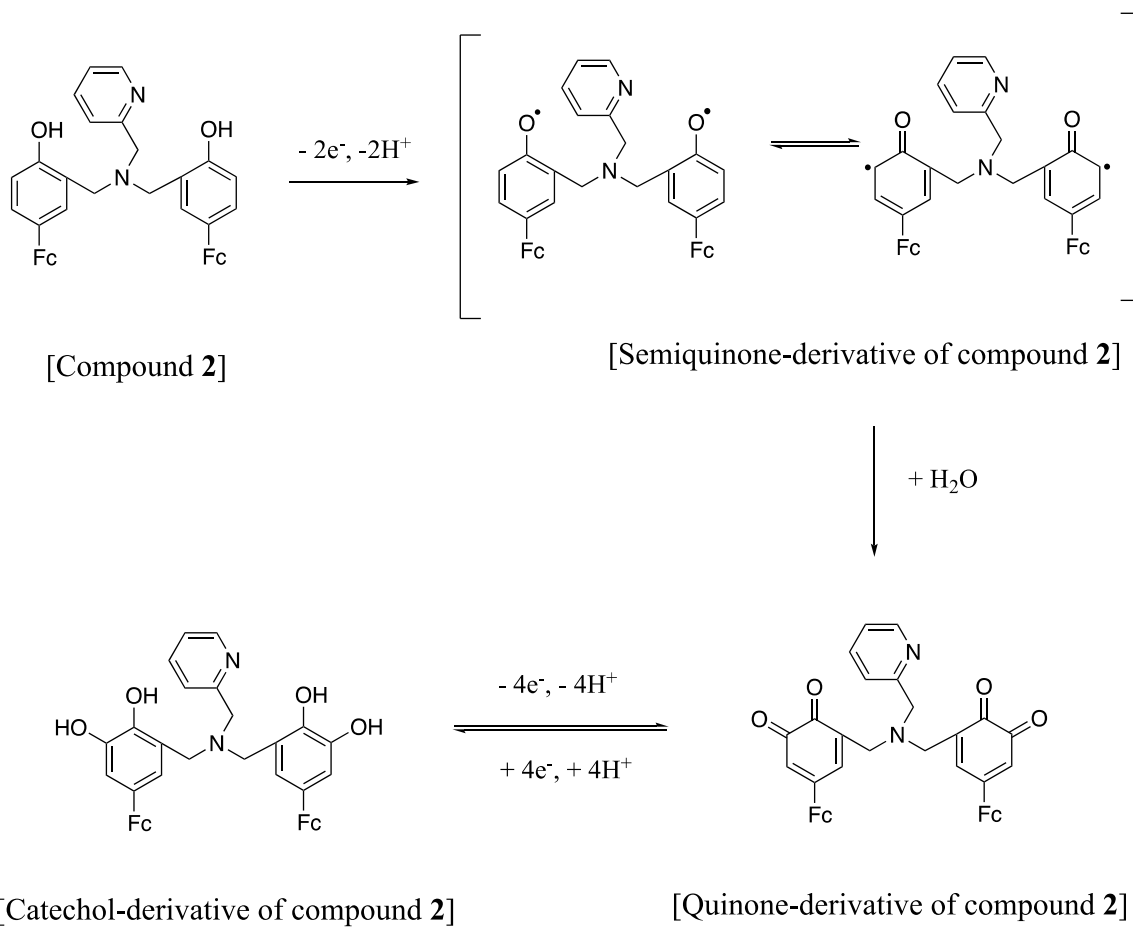
Figure 3.13 The cyclic voltammogram of compound **2** (5 mM) was recorded in dichloromethane (DCM) of solution of tetra-n-butylammonium hexafluorophosphate [ⁿBu₄N][PF₆] (0.1 M). Scan rate: 100 mV/s. Potential versus Fc⁺/Fc.

Table 3.9 The calculation of half-wave potential of compound **2** versus Fc^+/Fc .

The calculation of half-wave potential of compound 2 versus Fc^+/Fc		
	Current (μA)	Potential (mV)
Reduction peak	-8.02	0.0314
Oxidation peak	2.62	0.0278
Half-wave potential	-2.69	0.0296

The proposed mechanism for electrochemical oxidation and reduction of compound **2** is shown in **Scheme 3.2**, based on previous studies by others on phenol.⁷² In this condition, compound **2** undergoes oxidation in a two-step peak at $E_{\text{ox1}} = +1.20$ V and $E_{\text{ox2}} = +1.60$ V. That is results in the transfer of two electrons and two protons incompletely from compound **2** to quinone-derivative of compound **2**. The second oxidation peak occurred in the CV because compound **2** is not completely oxidized at the lower voltage. On the reverse scan, a single strong reduction peak occurred at $E_{\text{red}} = -1.40$ V (same as the compound **1**). The cathodic peak potentially corresponds to the reduction of quinone-derivative of compound **2** (two phenol oxidation products) to catechol-derivative of compound **2**, and includes transfer as well as receipt of four electrons and four protons.

Further analytical experiments are required in the future to confirm formation of the catechism derivative, for example using mass spectrometry.



Scheme 3.2 Proposed mechanism for electrochemical oxidation of compound 2 via cyclic voltammogram.

Table 3.10 The calculation and summarize of the half-wave potential of ferrocene, compound **1**, compound **2** before and after correction (versus Fc^+/Fc).

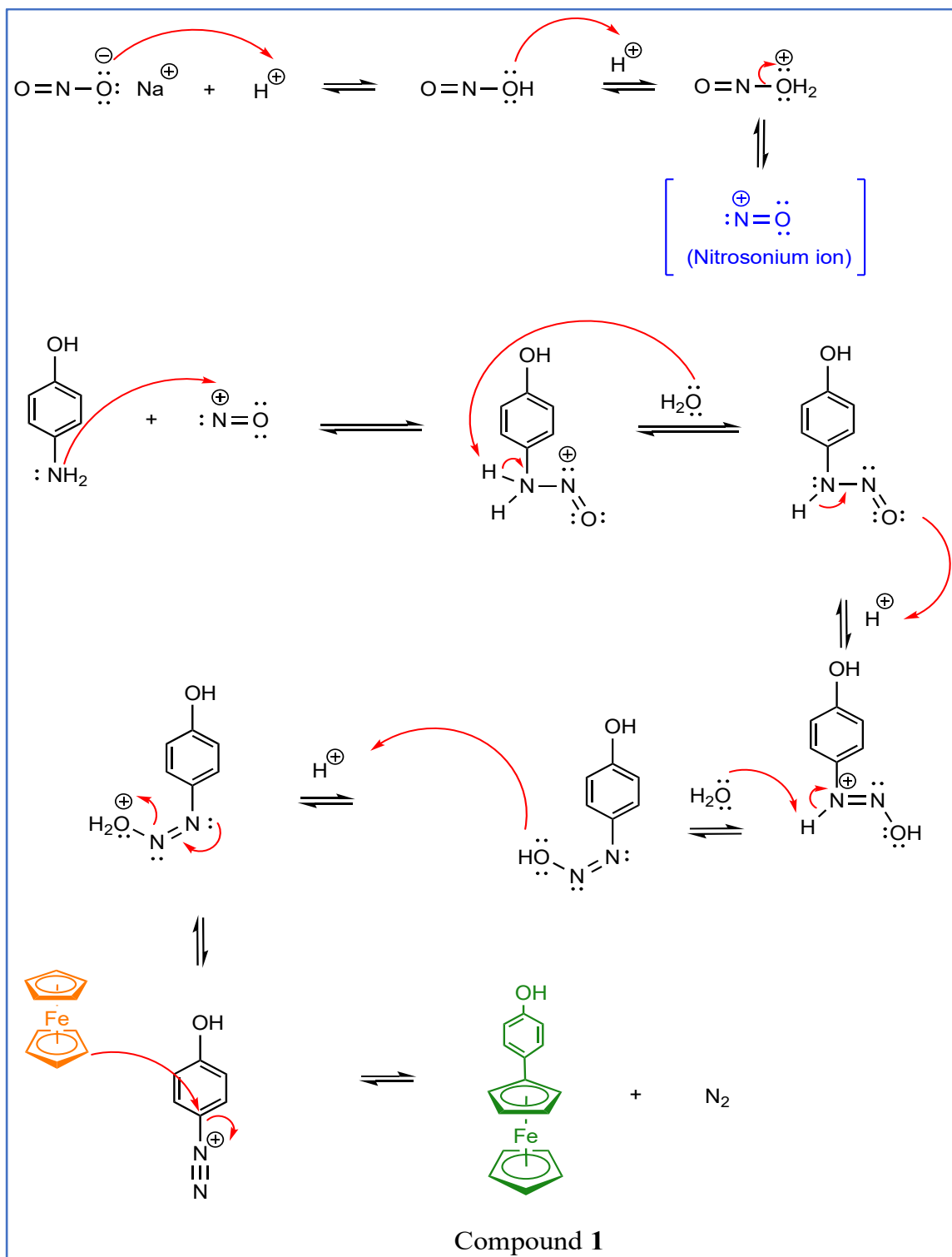
	Ferrocene (Fc) (mV)	Compound 1 (mV)	Compound 2 (mV)
Raw data	+49.6	-0.0345	+0.0296
After correction (vs. Fc^+/Fc)	0.00	-49.6	-49.6

The selection of ferrocene as an external reference standard holds significant importance in electrochemical studies. By designating the half-wave potential of ferrocene as 0.00 mV, a benchmark is established against which the half-wave potentials of other compounds can be compared. In this context, compound **1** and compound **2** exhibit half-wave potentials of -49.6 mV each (**Table 3.10**). The equalization of the corrected half-wave potentials of compound **1** and compound **2** signifies an intriguing finding. It suggests that alternative functional groups present in these compounds do not exert any discernible influence on the ferrocene moieties redox couple. The utilization of ferrocene as a reference compound simplifies the interpretation of electrochemical data by providing a well-defined baseline for comparison. It allows one to do quick comparisons, especially in exotic solvents which don't have a readily available reference electrode.

3.3 Reaction mechanism

3.3.1 Mechanism of synthesis of 1-ferrocenyl-4-hydroxybenzene

This reaction enables the incorporation of an aryl group onto the ferrocene ring system. To initiate the process, an arylamine (Ar-NH_2) undergoes treatment with nitrous acid (HNO_2) to form a diazonium salt. Due to its instability, the diazonium salt acts as an electrophile, attacking the ferrocene ring system, which is composed of two fused aromatic rings. As a result, one of the hydrogen atoms on the ferrocene ring is replaced by the aryl group, leading to the formation of a ferrocene compound that is substituted with an aryl group (**Scheme 3.3**). The low yield of the reaction can be attributed to the exceptional stability of ferrocene,¹² rendering it challenging to react with the given reactants. Consequently, achieving a satisfactory yield becomes arduous as the reactivity of ferrocene remains limited.

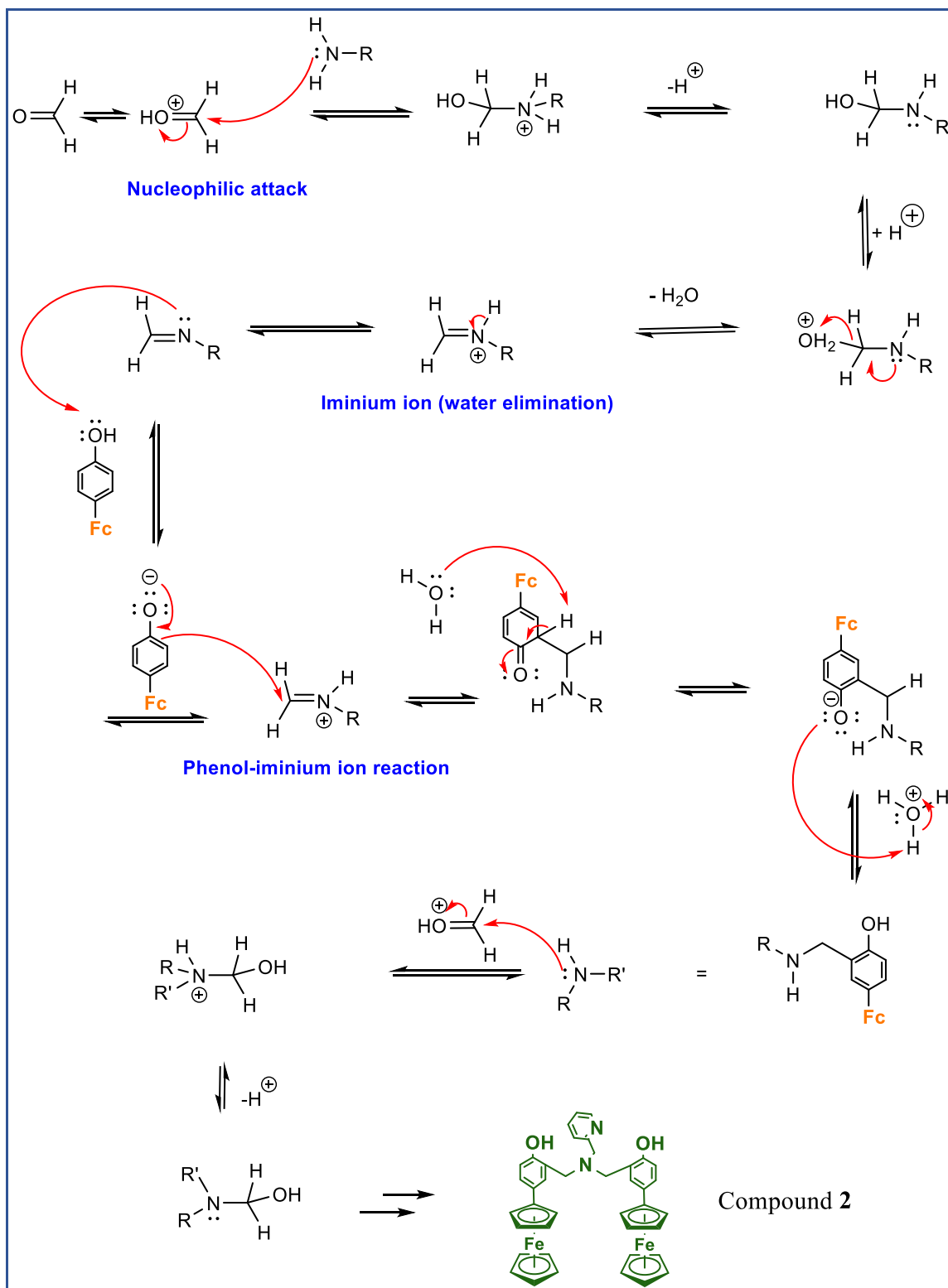


Scheme 3.3 The mechanism of synthesis of compound 1.

3.3.2 Mechanism of synthesis of a ferrocene-containing aminophenol

The description of the reaction mechanism for synthesizing compound **2** can be found in **Scheme 3.4**. In the first step, the carbonyl compound (formaldehyde) is protonated at the oxygen atom, making it more electrophilic. The protonated carbonyl compound then undergoes a nucleophilic attack by the nitrogen atom of the amine (2-picolyamine). The lone pair of electrons on the nitrogen attacks the electrophilic carbon of the carbonyl group, leading to the formation of a tetrahedral intermediate. This intermediate then undergoes a proton transfer from the nitrogen atom to the oxygen, resulting in the formation of an iminium ion.

The compound **1** loses a proton to the imine nitrogen generating a conjugate base which is capable of acting as a nucleophile. The enolate, formed from compound **1**, attacks the electrophilic carbon of the iminium ion, leading to the formation of the ferrocene-containing aminophenol product. Finally, to obtain the final product, the aminophenol undergoes deprotonation.



Scheme 3.4 The mechanism of synthesis of compound **2**.

Chapter 4: Conclusions and Future Work

The development of new ligands for metal catalysts is a crucial area of research in the field of chemistry, as it can lead to the synthesis of new molecules with unique properties. For this thesis, a new ferrocene-containing aminophenol ligand was successfully synthesized, which was thoroughly characterized using several analytical techniques. One of the most commonly used techniques to characterize organic molecules is Nuclear Magnetic Resonance (NMR) spectroscopy. The synthesized ligand was analyzed using NMR, which provided valuable information about its chemical structure and confirmed the successful synthesis of the ligand. Matrix-assisted laser desorption/ionization time-of-flight mass spectrometry (MALDI-TOF MS) was used to determine the molecular weight of the synthesized ligand. The results obtained from this technique provided further confirmation of the successful synthesis of the ligand and its purity. To further verify the molecular structure and crystal structure of the synthesized ligand, X-ray crystallography was employed. This technique provided a detailed picture of the ligand's molecular structure, including its orientation and bonding geometry. Finally, UV-Vis spectroscopies were used to investigate the ligand's electronic properties. This technique provided insights into the

electronic transitions occurring in the synthesized ligand, further confirming its suitability as a metal catalyst ligand.

The electrochemical behavior of a system can provide valuable insights into its properties and behavior. In this particular study, the potential state of the system was evaluated using cyclic voltammetry methods, which involves applying a voltage to the system and measuring the resulting current. By doing so, we were able to investigate the behavior of the Fc^+/Fc couple which refers to the ferrocenium/ferrocene redox couple - a commonly used reference standard in electrochemistry. It is a reversible redox couple, meaning that the system can easily switch between the oxidized (Fc^+) and reduced (Fc) states, depending on the applied potential. The results of the cyclic voltammetry measurements provide important information about the behavior of the Fc^+/Fc couple. The results of this study can be used to inform future research and design efforts in the field of electrochemistry.

In future research, when exposed to metal, compound **2** undergoes a transformation into phenolate, which comprises a novel series of metal complexes featuring a ferrocene-based aminophenolate ligand (**Figure 4.1**). The metals selected for complexation include Ti, Zr, Fe, Co, and Al. These metal complexes are expected to serve as efficient catalysts for ring-opening polymerizations (ROP) and ring-opening copolymerizations (ROCOP),

with potential applications in the synthesis of new materials. The unique properties of ferrocene-containing aminophenol ligands, such as their redox activity and chelating ability, make them suitable for metal complexation and catalytic applications. The success of this research could lead to the development of new and improved catalysts for the synthesis of polymers and copolymers with tailored properties.

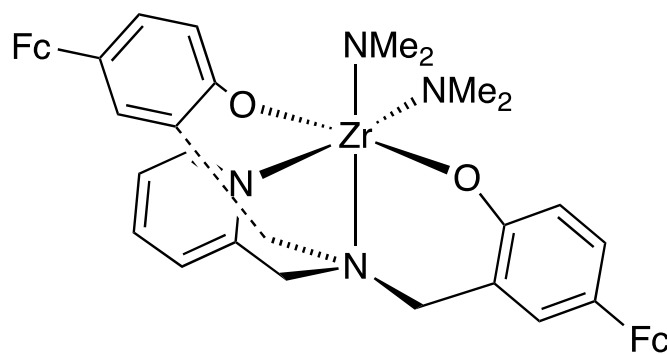


Figure 4.1 Example of possible complex with ferrocene containing aminophenolate ligand derived from compound **2**.

References

1. Kealy, T. J., and Pauson, P. L. A new type of organo-iron compound. *Nature* **168** 1039–1040 (1951).
2. Wilkinson, G., Rosenblum, M., C. Whiting, M., and B. Woodward, R. The structure of iron bis-cyclopentadienyl. *J. Am. Chem. Soc.* **74**, 2125–2126 (2002).
3. Rosenblum, M., and B. Woodward, R. The structure and chemistry of ferrocene. III. Evidence pertaining to the ring rotational barrier. *J. Am. Chem. Soc.* **80**, 5443–5449 (2002).
4. <https://www.nobelprize.org/prizes/chemistry/1973/summary/>.
5. Larik, F. A., Saeed, A., Fattah, T. A., Muqadar, U., and Channar, P. A. Recent advances in the synthesis, biological activities and various applications of ferrocene derivatives. *Appl. Organomet. Chem.* **31**, 3664 (2017).
6. Pal, A., Ranjan Bhatta, S., and Thakur, A. Recent advances in the development of ferrocene based electroactive small molecules for cation recognition: A comprehensive review of the years 2010–2020. *Coord. Chem. Rev.* **431**, 213685 (2021).
7. Hu, M.-L. *et al.* Electrochemical applications of ferrocene-based coordination polymers. *Chempluschem* **85**, 2397–2418 (2020).
8. Patra, M., and Gasser, G. The medicinal chemistry of ferrocene and its derivatives. *Nat. Rev. Chem.* **1**, 66 (2017).
9. Fouda, M. F. R., Abd-Elzaher, M. M., Abdelsamaia, R. A., and Labib, A. A. On the medicinal chemistry of ferrocene. *Appl. Organomet. Chem.* **21**, 613–625 (2007).

10. Takahashi, S., and Anzai, J. I. Recent progress in ferrocene-modified thin films and nanoparticles for biosensors. *Materials* **6**, 5742–5762 (2013).
11. Castagnola, M., Floris, B., Illuminati, G., and Ortaggi, G. The electron donor properties of ferrocene. The oxidation of ferrocene by carboxylic acids. *J. Organomet. Chem.* **60**, C17–C18 (1973).
12. Astruc, D. Why is ferrocene so exceptional? *Eur. J. Inorg. Chem.* **2017**, 6–29 (2017).
13. Wang, R. *et al.* Ferrocene-containing hybrids as potential anticancer agents: Current developments, mechanisms of action and structure-activity relationships. *Eur. J. Med. Chem.* **190**, 112109 (2020).
14. Peter, S., and Aderibigbe, B. A. Ferrocene-based compounds with antimalaria/anticancer activity. *Molecules* **24**, 3604 (2019).
15. Ornelas, C. Application of ferrocene and its derivatives in cancer research. *New J. Chem.* **35**, 1973–1985 (2011).
16. Neuse, E. W. Macromolecular ferrocene compounds as cancer drug models. *J. Inorg. Organomet. Polym. Mater.* **15**, 3–31 (2005).
17. Rabti, A., Mayorga-Martinez, C. C., Baptista-Pires, L., Raouafi, N., and Merkoçi, A. Ferrocene-functionalized graphene electrode for biosensing applications. *Anal. Chim. Acta* **926**, 28–35 (2016).
18. Guan, L., Shi, Z., Li, M., and Gu, Z. Ferrocene-filled single-walled carbon nanotubes. *Carbon* **43**, 2780–2785 (2005).
19. Sarhan, A. E.-W. A. O. Synthesis and applications of tetrathiafulvalenes and ferrocene-tetrathiafulvalenes and related compounds. *Tetrahedron* **61**, 3889–3932 (2005).

20. Rabti, A., Raouafi, N., and Merkoçi, A. Bio (sensing) devices based on ferrocene-functionalized graphene and carbon nanotubes. *Carbon* **108**, 481–514 (2016).
21. Khan, A. *et al.* Research advances in the synthesis and applications of ferrocene-based electro and photo responsive materials. *Appl. Organomet. Chem.* **32**, 4575 (2018).
22. Fabbrizzi, L. The ferrocenium/ferrocene couple: a versatile redox switch. *ChemTexts* **6**, 22 (2020).
23. Skinner, H. A. The strengths of metal-to-carbon bonds. *Adv. Organomet. Chem.* **2** 49–114 (1965).
24. Holloway, J. D. L., and Geiger Jr, W. E. Electron-transfer reactions of metallocenes. Influence of metal oxidation state on structure and reactivity. *J. Am. Chem. Soc.* **101**, 2038–2044 (1979).
25. Choudhury, J. Recent developments on artificial switchable catalysis. *Tetrahedron Lett.* **59**, 487–495 (2018).
26. Gutiérrez-Peña, C. L., Poyatos, M., and Peris, E. A redox-switchable catalyst with an ‘unplugged’ redox tag. *Chem. Commun.* **58**, 10564–10567 (2022).
27. Rosas-Hernández, A., Junge, H., Beller, M., Roemelt, M., and Francke, R. Cyclopentadienone iron complexes as efficient and selective catalysts for the electroreduction of CO₂ to CO. *Catal. Sci. Technol.* **7**, 459–465 (2017).
28. Zhao, Y. *et al.* A supramolecular approach to construct a hydrolase mimic with photo-switchable catalytic activity. *J. Mater. Chem. B* **6**, 2444–2449 (2018).
29. Baruah, M. J. *et al.* Boosting multiple photo-assisted and temperature controlled reactions with a single redox-switchable catalyst: Solvents as internal substrates and reducing agent. *J. Catal.* **388**, 104–121 (2020).

30. Wuerthner, F., and Rebek Jr, J. Light-switchable catalysis in synthetic receptors. *Angew. Chem., Int. Ed. Engl.* **34**, 446–448 (1995).
31. Hou, J. *et al.* Supramolecularly regulated artificial transmembrane signal transduction for 'ON/OFF'-switchable enzyme catalysis. *Chem. Commun.* **58**, 5725–5728 (2022).
32. Li, X. *et al.* Switchable enzyme mimics based on self-assembled peptides for polyethylene terephthalate degradation. *J. Colloid Interface Sci.* **646**, 198–208 (2023).
33. Durola, F. *et al.* Cyclic [4] rotaxanes containing two parallel porphyrinic plates: Toward switchable molecular receptors and compressors. *Acc. Chem. Res.* **47**, 633–645 (2014).
34. Teimuri-Mofrad, R., Abbasi, H., and Hadi, R. Graphene oxide-grafted ferrocene moiety via ring opening polymerization (ROP) as a supercapacitor electrode material. *Polymer* **167**, 138–145 (2019).
35. Lai, A., Hern, Z. C., and Diaconescu, P. L. Switchable ring-opening polymerization by a ferrocene supported aluminum complex. *ChemCatChem* **11**, 4210–4218 (2019).
36. Wang, X. *et al.* Redox control of group 4 metal ring-opening polymerization activity toward L-lactide and ϵ -caprolactone. *J. Am. Chem. Soc.* **136**, 11264–11267 (2014).
37. Buretea, M. A., and Tilley, T. D. Poly (ferrocenylenevinylene) from ring-opening metathesis polymerization of ansa-(vinylene) ferrocene. *Organometallics* **16**, 1507–1510 (1997).
38. Broderick, E. M. *et al.* Redox control of a ring-opening polymerization catalyst. *J. Am. Chem. Soc.* **133**, 9278–9281 (2011).
39. Wei, J., and Diaconescu, P. L. Redox-switchable ring-opening polymerization with ferrocene derivatives. *Acc. Chem. Res.* **52**, 415–424 (2019).

40. Hermans, C., Rong, W., Spaniol, T. P., and Okuda, J. Lanthanum complexes containing a bis (phenolate) ligand with a ferrocene-1, 1'-diyldithio backbone: synthesis, characterization, and ring-opening polymerization of rac-lactide. *Dalton Trans.* **45**, 8127–8133 (2016).
41. K. A. Gregson, C. *et al.* Redox control within single-site polymerization catalysts. *J. Am. Chem. Soc.* **128**, 7410–7411 (2006).
42. Wang, X. *et al.* Redox control of group 4 metal ring-opening polymerization activity toward l-lactide and ϵ -caprolactone. *J. Am. Chem. Soc.* **136**, 11264–11267 (2014).
43. Podolan, G., Hettmanczyk, L., Hommes, P., Sarkar, B., and Reissig, H. Synthesis and (spectro) electrochemistry of ferrocenyl-substituted pyridine derivatives. *Eur. J. Org. Chem.* **2015**, 7317–7323 (2015).
44. Karagollu, O., Gorur, M., Gode, F., Sennik, B., and Yilmaz, F. Phosphate ion sensors based on triazole connected ferrocene moieties. *Sens. Actuators B Chem.* **193**, 788–798 (2014).
45. <https://www.nobelprize.org/prizes/chemistry/2022/summary/>.
46. Mou, R.-Q., Zhao, M., Lv, X.-X., Zhang, S.-Y., and Guo, D.-S. An efficient and green synthesis of ferrocenyl-quinoline conjugates via a TsOH-catalyzed three-component reaction in water. *RSC Adv.* **8**, 9555–9563 (2018).
47. Hayat, F., Azam, A., and Shin, D. Recent progress on the discovery of antiameobic agents. *Bioorg. Med. Chem. Lett.* **26**, 5149–5159 (2016).
48. Yang, F. *et al.* Synthesis and nonlinear optical absorption properties of two new conjugated ferrocene-bridge-pyridinium compounds. *Tetrahedron* **63**, 9188–9194 (2007).
49. Montes-González, I., Alsina-Sánchez, A. M., Aponte-Santini, J. C., Delgado-Rivera, S. M., and Durán-Camacho, G. L. Perspectives of ferrocenyl chalcones: synthetic scaffolds

- toward biomedical and materials science applications. *Pure and Appl. Chem.* **91**, 653–669 (2019).
50. Dolomanov, O. V, Bourhis, L. J., Gildea, R. J., Howard, J. A. K., and Puschmann, H. OLEX2: a complete structure solution, refinement and analysis program. *J. Appl. Crystallogr.* **42**, 339–341 (2009).
 51. Sheldrick, G. M. SHELXT—Integrated space-group and crystal-structure determination. *Acta Crystallogr. A: Found. Adv.* **71**, 3–8 (2015).
 52. Sheldrick, G. M. Crystal structure refinement with SHELXL. *Acta Crystallogr. C Struct. Chem.* **71**, 3–8 (2015).
 53. Sumner, J. J., and Creager, S. E. Topological effects in bridge-mediated electron transfer between redox molecules and metal electrodes. *J. Am. Chem. Soc.* **122**, 11914–11920 (2000).
 54. <https://pineresearch.com/shop/products/potentiostats/wavenow-series/wavenow-wireless/#documentation>.
 55. Karas, M., Bachmann, D., Bahr, U., and Hillenkamp, F. Matrix-assisted ultraviolet laser desorption of non-volatile compounds. *Int. J. Mass Spectrom. Ion Process* **78**, 53–68 (1987).
 56. Karas, M., and Hillenkamp, F. Laser desorption ionization of proteins with molecular masses exceeding 10,000 daltons. *Anal. Chem.* **60**, 2299–2301 (1988).
 57. Stahl, B., Linos, A., Karas, M., Hillenkamp, F., and Steup, M. Analysis of fructans from higher plants by matrix-assisted laser desorption/ionization mass spectrometry. *Anal. Biochem.* **246**, 195–204 (1997).

58. Dreisewerd, K., Schürenberg, M., Karas, M., and Hillenkamp, F. Matrix-assisted laser desorption/ionization with nitrogen lasers of different pulse widths. *Int. J. Mass Spectrom. Ion Process* **154**, 171–178 (1996).
59. Jones, R. N. The ultraviolet absorption spectra of anthracene derivatives. *Chem. Rev.* **41**, 353–371 (1947).
60. Eelman, M. D., Blacquiere, J. M., Moriarty, M. M., and Fogg, D. E. Shining new light on an old problem: retooling MALDI mass spectrometry for organotransition-metal catalysis. *Angew. Chem.* **120**, 309–312 (2008).
61. Ikpo, N., Butt, S. M., Collins, K. L., and Kerton, F. M. A study of ligand coordination at lanthanide and group 4 metal centers by matrix-assisted laser desorption/ionization time-of-flight mass spectrometry. *Organometallics* **28**, 837–842 (2009).
62. Wang, J., Kalt, W., and Sporns, P. Comparison between HPLC and MALDI-TOF MS analysis of anthocyanins in highbush blueberries. *J. Agric. Food Chem.* **48**, 3330–3335 (2000).
63. Woolfson, M. M. An introduction to X-ray crystallography. *Cambridge University Press* (1997).
64. https://www.iucr.org/iycr_orig.
65. Smyth, M. S., and Martin, J. H. J. X-ray crystallography. *Mol. Pathol.* **53**, 8 (2000).
66. Karplus, P. A., and Diederichs, K. Linking crystallographic model and data quality. *Science* **336**, 1030–1033 (2012).
67. Diederichs, K., and Karplus, P. A. Improved R-factors for diffraction data analysis in macromolecular crystallography. *Nat. Struct. Biol.* **4**, 269–275 (1997).

68. Elgrishi, N. *et al.* A practical beginner's guide to cyclic voltammetry. *J. Chem. Educ.* **95**, 197–206 (2018).
69. CH, V., Srividya, A., Ajitha, A., and Rao, U. An overview on cyclic voltammetry and its application in pharmaceutical analysis. *Int. J. Chem. Pharm. Sci* **5**, (2014).
70. Smit, S. M., Buisman, C. J. N., Bitter, J. H., and Strik, D. P. Cyclic voltammetry is invasive on microbial electrosynthesis. *ChemElectroChem* **8**, 3384–3396 (2021).
71. Gulaboski, R., Kokoskarova, P., and Petkovska, S. Analysis of drug-drug interactions with cyclic voltammetry: An overview of relevant theoretical models and recent experimental achievements. *Anal. Bioanal. Electrochem.* **12**, 345–364 (2020).
72. Enache, T. A., and Oliveira-Brett, A. M. Phenol and para-substituted phenols electrochemical oxidation pathways. *J. Electroanal. Chem.* **655**, 9–16 (2011).

Appendix

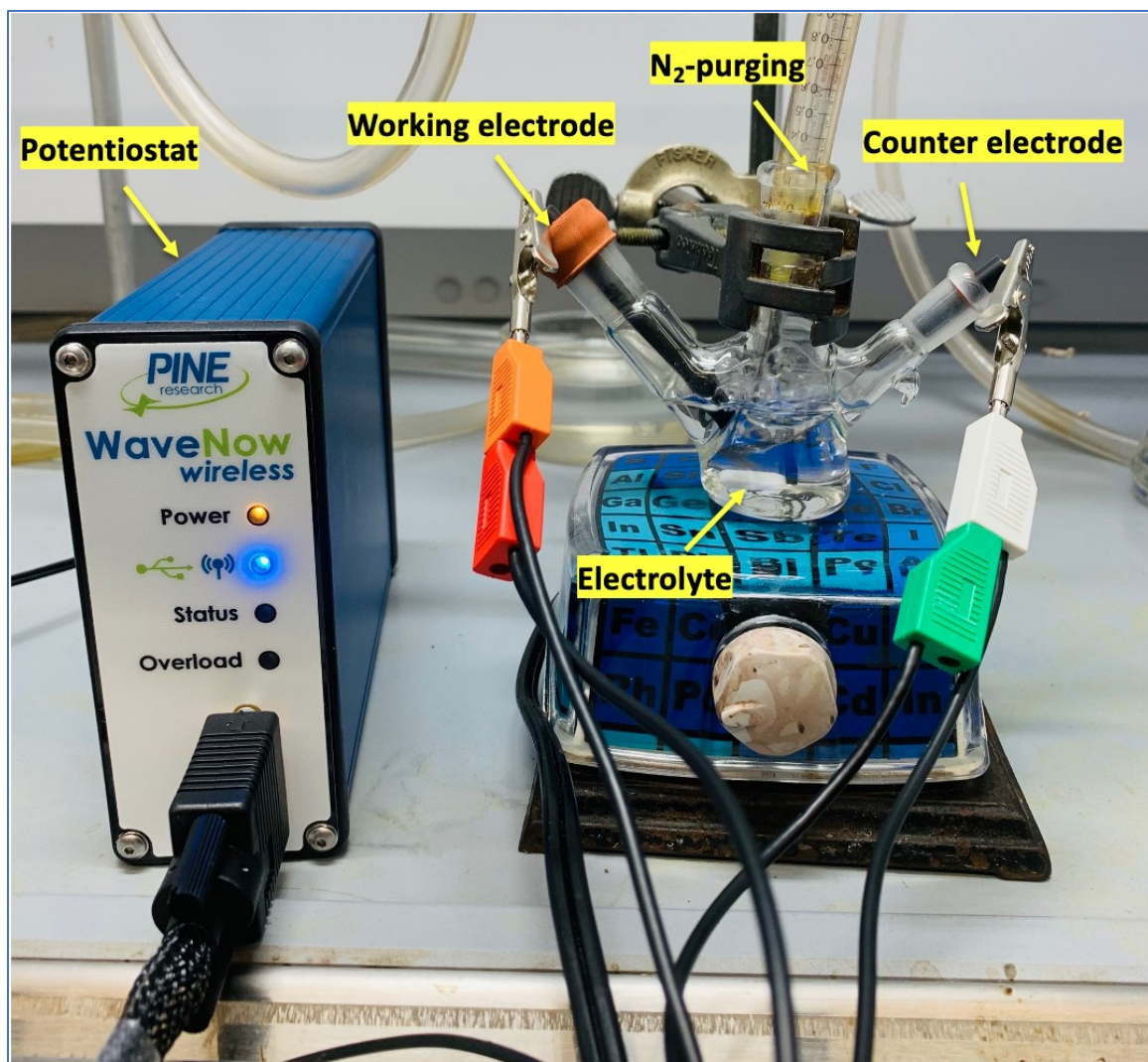


Figure A.1 Procedure for setting up the CV experiment.

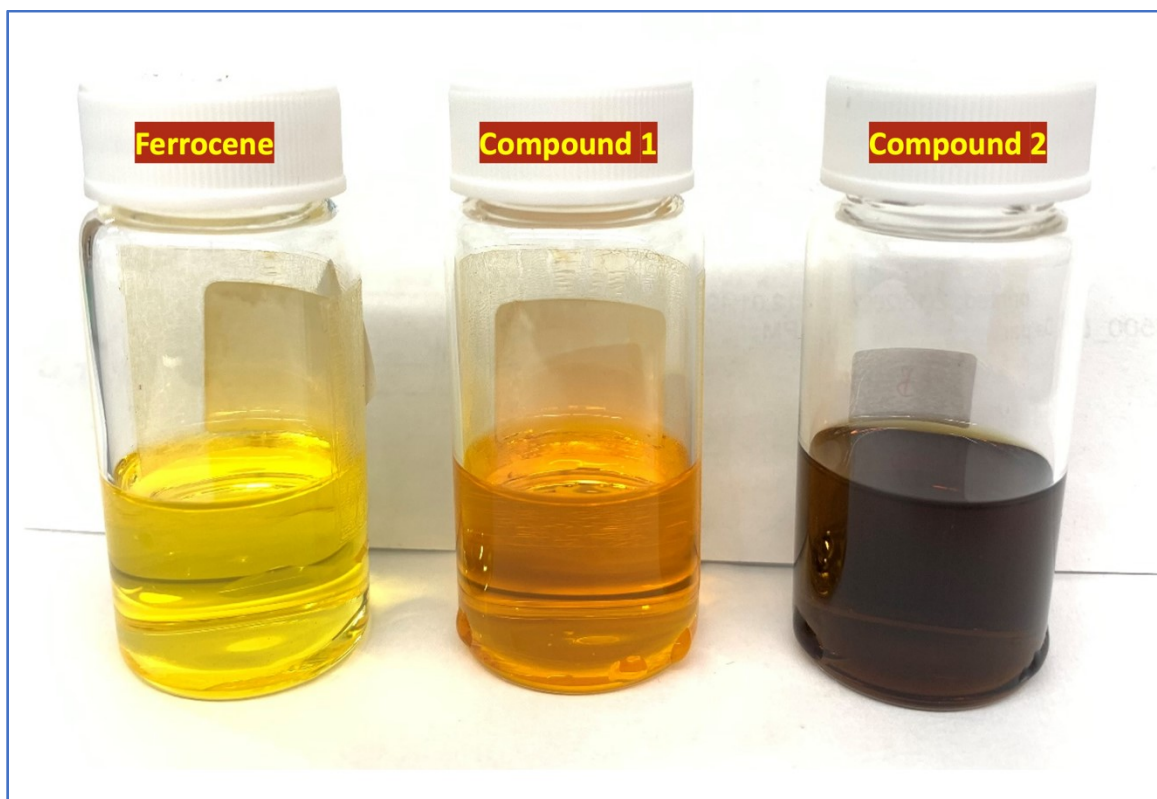


Figure A.2 The different colour of ferrocene, compound 1, and compound 2 when they are diluted in dichloromethane (DCM) at the concentration of 5 mM (room temperature).

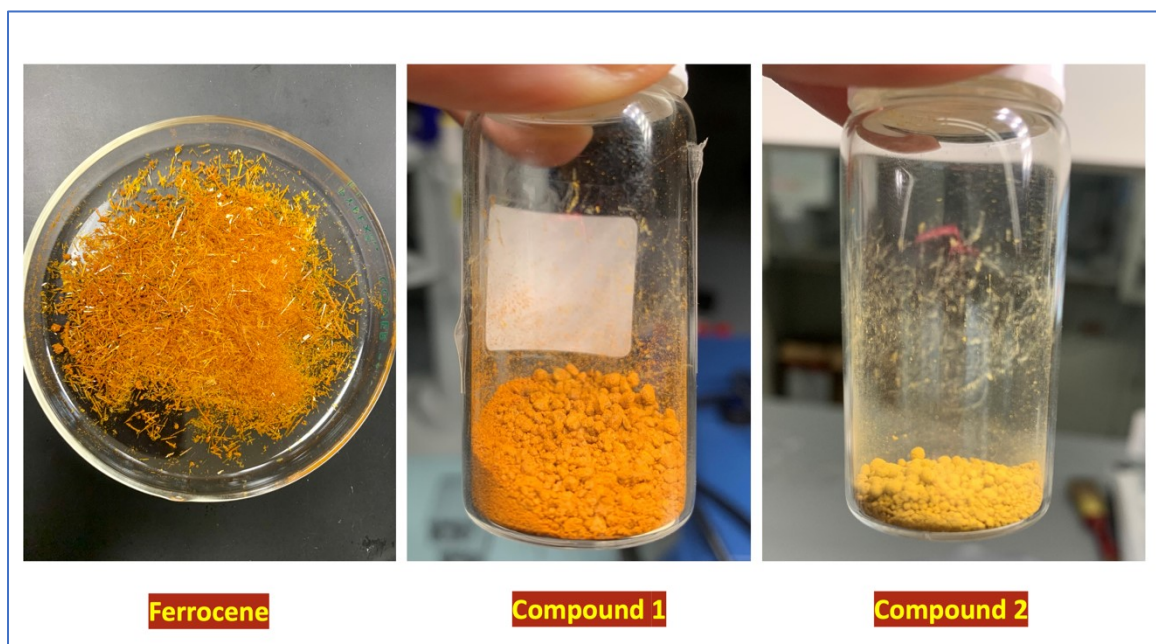


Figure A.3 The different colour of ferrocene, compound 1, and compound 2 in solid state at room temperature.

Table A.1 The elemental analysis of compound **2** (C₄₀H₃₆Fe₂N₂O₂).

Element	Calculated	Found
C	69.77	68.75
H	5.23	5.22
N	4.07	5.09

Table A.2 Fractional Atomic Coordinates ($\times 10^4$) and Equivalent Isotropic Displacement Parameters ($\text{\AA}^2 \times 10^3$). U_{eq} is defined as 1/3 of the trace of the orthogonalised U_{IJ} tensor.

Atom	x	y	z	$U(\text{eq})$
Fe1	8663.4(2)	4015.9(8)	8309.4(2)	40.98(15)
Fe2	3549.6(3)	3768.9(9)	5580.9(2)	49.94(17)
O1	5671.8(13)	8042(4)	8711.7(10)	56.2(6)
O2	4096.0(17)	7990(6)	8160.3(13)	74.0(8)
N1	5105.6(14)	4166(5)	8434.5(11)	48.4(6)
N2	4309.2(16)	5658(6)	9078.0(13)	63.9(8)
C1	8533(2)	3271(7)	7531.2(14)	65.3(11)
C2	9176(2)	3962(9)	7727.1(18)	76.5(14)
C3	9132(2)	6142(8)	7914.2(15)	68.8(12)
C4	8488(2)	6745(6)	7840.9(13)	57.1(9)
C5	8114.0(18)	4987(7)	7603.2(12)	55.8(9)
C6	8715.0(17)	4882(6)	9071.8(12)	49.0(7)
C7	9203.4(18)	3337(6)	9037.1(13)	53.3(8)
C8	8910.4(18)	1388(6)	8807.1(14)	51.2(8)
C9	8227.9(17)	1716(5)	8698.2(13)	46.2(7)
C10	8093.2(16)	3898(5)	8860.5(11)	42.6(7)
C11	7456.7(16)	4926(5)	8823.1(11)	42.6(7)
C12	6889.1(16)	3878(5)	8573.2(11)	42.3(7)
C13	6281.5(16)	4845(5)	8528.7(11)	44.2(7)
C14	6246.6(16)	6970(5)	8749.6(12)	44.9(7)
C15	6802.9(17)	8004(5)	9005.1(13)	47.9(7)
C16	7397.8(17)	7007(6)	9045.6(12)	46.6(7)

Atom	<i>x</i>	<i>y</i>	<i>z</i>	U(eq)
C17	5695.6(17)	3727(5)	8225.2(12)	47.3(7)
C18	4530.5(18)	3449(6)	8045.7(14)	52.7(8)
C19	4359.4(17)	5053(6)	7599.7(14)	54.1(8)
C20	4150(2)	7184(7)	7680.8(15)	61.2(9)
C21	3974(2)	8610(7)	7257.3(17)	67.3(11)
C22	4018(2)	7932(7)	6757.9(16)	64.9(10)
C23	4225.2(18)	5829(6)	6661.7(14)	55.1(8)
C24	4390.4(17)	4426(6)	7093.9(14)	52.4(8)
C25	4279.6(16)	5124(7)	6135.6(14)	53.2(8)
C26	4142.9(18)	6451(7)	5664.2(15)	58.8(9)
C27	4252.9(18)	5146(8)	5242.8(14)	62.6(10)
C28	4449.4(17)	2964(7)	5436.6(14)	58.1(9)
C29	4462.9(16)	2981(7)	5979.7(13)	54.6(8)
C30	2718.0(19)	3842(10)	5864.9(17)	76.1(14)
C31	2899(2)	1600(9)	5782(2)	76.4(13)
C32	2921(2)	1371(7)	5255.9(19)	66.4(10)
C33	2749.6(17)	3363(7)	5006.2(14)	55.4(8)
C34	2620.3(17)	4930(7)	5370.9(15)	57.8(9)
C35	5134.1(18)	3000(6)	8931.9(13)	50.9(8)
C36	4633.7(18)	3769(7)	9227.8(14)	56.0(9)
C37	4528(2)	2518(9)	9647.2(17)	74.2(12)
C38	4090(2)	3236(12)	9938.0(19)	91.7(17)
C39	3758(2)	5226(12)	9788.7(19)	92.2(18)
C40	3877(2)	6341(9)	9359(2)	79.7(14)
O3	2412(18)	1130(100)	7138(15)	310(20)

Atom	<i>x</i>	<i>y</i>	<i>z</i>	U(eq)
C41	2504(13)	-230(80)	7594(18)	215(17)
C42	2940(20)	850(100)	8061(16)	290(20)
O3A	2671(6)	3310(40)	7278(6)	194(8)
C41A	2634(12)	2290(60)	7759(7)	230(12)
C42A	2844(6)	3040(40)	8319(6)	171(9)

Table A.3 Selected Bond Distances (Å) of compound **2**.

Atom	Atom	Length/Å	Atom	Atom	Length/Å
Fe1	C1	2.044(4)	C9	C10	1.431(5)
Fe1	C2	2.033(4)	C10	C11	1.464(5)
Fe1	C3	2.025(4)	C11	C12	1.395(5)
Fe1	C4	2.042(4)	C11	C16	1.401(5)
Fe1	C5	2.057(3)	C12	C13	1.391(5)
Fe1	C6	2.039(3)	C13	C14	1.416(5)
Fe1	C7	2.051(3)	C13	C17	1.489(5)
Fe1	C8	2.052(3)	C14	C15	1.378(5)
Fe1	C9	2.043(3)	C15	C16	1.376(5)
Fe1	C10	2.052(3)	C18	C19	1.502(5)
Fe2	C25	2.060(3)	C19	C20	1.392(6)
Fe2	C26	2.032(4)	C19	C24	1.387(5)
Fe2	C27	2.047(4)	C20	C21	1.392(6)
Fe2	C28	2.064(4)	C21	C22	1.387(6)
Fe2	C29	2.054(3)	C22	C23	1.383(6)
Fe2	C30	2.035(4)	C23	C24	1.398(5)
Fe2	C31	2.040(4)	C23	C25	1.464(5)
Fe2	C32	2.031(4)	C25	C26	1.448(5)
Fe2	C33	2.036(3)	C25	C29	1.434(6)
Fe2	C34	2.050(4)	C26	C27	1.410(6)
O1	C14	1.360(4)	C27	C28	1.443(6)
O2	C20	1.368(5)	C28	C29	1.412(5)
N1	C17	1.479(4)	C30	C31	1.435(7)
N1	C18	1.482(4)	C30	C34	1.425(6)

Atom	Atom	Length/Å	Atom	Atom	Length/Å
N1	C35	1.468(4)	C31	C32	1.390(7)
N2	C36	1.348(5)	C32	C33	1.382(6)
N2	C40	1.344(5)	C33	C34	1.407(6)
C1	C2	1.413(7)	C35	C36	1.500(5)
C1	C5	1.399(6)	C36	C37	1.384(6)
C2	C3	1.415(7)	C37	C38	1.377(6)
C3	C4	1.382(6)	C38	C39	1.406(9)
C4	C5	1.393(6)	C39	C40	1.373(8)
C6	C7	1.406(5)	O3	C41	1.43(2)
C6	C10	1.445(5)	C41	C42	1.52(2)
C7	C8	1.408(5)	O3A	C41A	1.412(17)
C8	C9	1.424(5)	C41A	C42A	1.510(17)

Table A.4 Selected Bond Angles of compound **2**

Atom	Atom	Atom	Angle/°	Atom	Atom	Atom	Angle/°
C1	Fe1	C5	39.89(17)	C1	C2	C3	106.0(4)
C1	Fe1	C7	144.61(17)	C3	C2	Fe1	69.3(2)
C1	Fe1	C8	115.16(16)	C2	C3	Fe1	69.9(2)
C1	Fe1	C10	135.03(17)	C4	C3	Fe1	70.8(2)
C2	Fe1	C1	40.6(2)	C4	C3	C2	109.1(4)
C2	Fe1	C4	68.00(17)	C3	C4	Fe1	69.4(2)
C2	Fe1	C5	67.88(17)	C3	C4	C5	108.3(4)
C2	Fe1	C6	143.2(2)	C5	C4	Fe1	70.7(2)
C2	Fe1	C7	114.14(17)	C1	C5	Fe1	69.6(2)
C2	Fe1	C8	110.79(16)	C4	C5	Fe1	69.6(2)
C2	Fe1	C9	135.95(18)	C4	C5	C1	108.0(4)
C2	Fe1	C10	175.3(2)	C7	C6	Fe1	70.36(19)
C3	Fe1	C1	67.43(18)	C7	C6	C10	108.8(3)
C3	Fe1	C2	40.8(2)	C10	C6	Fe1	69.78(17)
C3	Fe1	C4	39.73(18)	C6	C7	Fe1	69.43(18)
C3	Fe1	C5	66.88(16)	C6	C7	C8	108.6(3)
C3	Fe1	C6	113.43(17)	C8	C7	Fe1	70.0(2)
C3	Fe1	C7	111.18(16)	C7	C8	Fe1	69.90(19)
C3	Fe1	C8	136.53(17)	C7	C8	C9	108.0(3)
C3	Fe1	C9	176.40(18)	C9	C8	Fe1	69.32(18)
C3	Fe1	C10	142.47(18)	C8	C9	Fe1	69.99(19)
C4	Fe1	C1	67.10(16)	C8	C9	C10	108.8(3)
C4	Fe1	C5	39.73(16)	C10	C9	Fe1	69.86(18)
C4	Fe1	C7	135.76(16)	C6	C10	Fe1	68.86(18)

Atom	Atom	Atom	Angle/°	Atom	Atom	Atom	Angle/°
C4	Fe1	C8	175.35(16)	C6	C10	C11	126.9(3)
C4	Fe1	C9	143.21(16)	C9	C10	Fe1	69.24(18)
C4	Fe1	C10	112.72(14)	C9	C10	C6	105.9(3)
C6	Fe1	C1	175.00(17)	C9	C10	C11	127.2(3)
C6	Fe1	C4	110.17(15)	C11	C10	Fe1	126.6(2)
C6	Fe1	C5	135.39(15)	C12	C11	C10	121.9(3)
C6	Fe1	C7	40.21(15)	C12	C11	C16	117.5(3)
C6	Fe1	C8	67.90(15)	C16	C11	C10	120.6(3)
C6	Fe1	C9	68.40(14)	C13	C12	C11	122.5(3)
C6	Fe1	C10	41.36(13)	C12	C13	C14	117.9(3)
C7	Fe1	C5	174.78(16)	C12	C13	C17	120.4(3)
C7	Fe1	C8	40.13(15)	C14	C13	C17	121.5(3)
C7	Fe1	C10	68.82(14)	O1	C14	C13	121.4(3)
C8	Fe1	C5	144.52(16)	O1	C14	C15	118.6(3)
C9	Fe1	C1	111.03(16)	C15	C14	C13	120.0(3)
C9	Fe1	C5	114.23(15)	C16	C15	C14	120.8(3)
C9	Fe1	C7	68.01(15)	C15	C16	C11	121.1(3)
C9	Fe1	C8	40.69(14)	N1	C17	C13	113.1(3)
C9	Fe1	C10	40.90(13)	N1	C18	C19	112.3(3)
C10	Fe1	C5	109.52(14)	C20	C19	C18	120.9(3)
C10	Fe1	C8	68.88(13)	C24	C19	C18	120.8(3)
C25	Fe2	C28	68.73(16)	C24	C19	C20	118.3(3)
C26	Fe2	C25	41.44(15)	O2	C20	C19	123.7(4)
C26	Fe2	C27	40.43(18)	O2	C20	C21	116.6(4)
C26	Fe2	C28	68.85(18)	C19	C20	C21	119.6(4)

Atom	Atom	Atom	Angle/°	Atom	Atom	Atom	Angle/°
C26	Fe2	C29	68.66(16)	C22	C21	C20	120.4(4)
C26	Fe2	C30	120.0(2)	C23	C22	C21	121.7(4)
C26	Fe2	C31	156.3(2)	C22	C23	C24	116.6(4)
C26	Fe2	C33	125.21(16)	C22	C23	C25	121.6(3)
C26	Fe2	C34	106.88(16)	C24	C23	C25	121.8(4)
C27	Fe2	C25	68.75(15)	C19	C24	C23	123.4(4)
C27	Fe2	C28	41.09(18)	C23	C25	Fe2	126.0(3)
C27	Fe2	C29	68.06(15)	C26	C25	Fe2	68.24(19)
C27	Fe2	C34	118.76(17)	C26	C25	C23	126.6(4)
C29	Fe2	C25	40.79(16)	C29	C25	Fe2	69.34(19)
C29	Fe2	C28	40.11(14)	C29	C25	C23	127.2(3)
C30	Fe2	C25	108.21(16)	C29	C25	C26	106.2(3)
C30	Fe2	C27	154.0(2)	C25	C26	Fe2	70.3(2)
C30	Fe2	C28	164.0(2)	C27	C26	Fe2	70.3(2)
C30	Fe2	C29	127.52(16)	C27	C26	C25	108.5(4)
C30	Fe2	C31	41.2(2)	C26	C27	Fe2	69.2(2)
C30	Fe2	C33	67.89(16)	C26	C27	C28	108.6(3)
C30	Fe2	C34	40.83(18)	C28	C27	Fe2	70.1(2)
C31	Fe2	C25	121.41(17)	C27	C28	Fe2	68.8(2)
C31	Fe2	C27	162.5(2)	C29	C28	Fe2	69.5(2)
C31	Fe2	C28	125.8(2)	C29	C28	C27	107.0(4)
C31	Fe2	C29	109.35(17)	C25	C29	Fe2	69.86(19)
C31	Fe2	C34	68.46(18)	C28	C29	Fe2	70.4(2)
C32	Fe2	C25	155.56(16)	C28	C29	C25	109.8(3)
C32	Fe2	C26	161.78(18)	C31	C30	Fe2	69.6(3)

Atom	Atom	Atom	Angle/°	Atom	Atom	Atom	Angle/°
C32	Fe2	C27	125.32(19)	C34	C30	Fe2	70.1(2)
C32	Fe2	C28	107.58(18)	C34	C30	C31	107.1(4)
C32	Fe2	C29	120.89(17)	C30	C31	Fe2	69.2(2)
C32	Fe2	C30	68.3(2)	C32	C31	Fe2	69.7(2)
C32	Fe2	C31	39.9(2)	C32	C31	C30	107.8(4)
C32	Fe2	C33	39.74(16)	C31	C32	Fe2	70.4(3)
C32	Fe2	C34	67.91(17)	C33	C32	Fe2	70.3(2)
C33	Fe2	C25	163.39(16)	C33	C32	C31	108.7(4)
C33	Fe2	C27	107.23(15)	C32	C33	Fe2	70.0(2)
C33	Fe2	C28	119.57(15)	C32	C33	C34	109.6(4)
C33	Fe2	C29	154.22(16)	C34	C33	Fe2	70.4(2)
C33	Fe2	C31	67.11(17)	C30	C34	Fe2	69.0(2)
C33	Fe2	C34	40.29(16)	C33	C34	Fe2	69.3(2)
C34	Fe2	C25	126.27(16)	C33	C34	C30	106.7(4)
C34	Fe2	C28	153.60(16)	N1	C35	C36	113.4(3)
C34	Fe2	C29	164.63(16)	N2	C36	C35	118.8(3)
C17	N1	C18	109.2(3)	N2	C36	C37	122.6(4)
C35	N1	C17	110.6(3)	C37	C36	C35	118.6(4)
C35	N1	C18	110.4(3)	C38	C37	C36	119.7(5)
C40	N2	C36	117.5(4)	C37	C38	C39	117.9(5)
C2	C1	Fe1	69.3(2)	C40	C39	C38	118.9(4)
C5	C1	Fe1	70.5(2)	N2	C40	C39	123.4(5)
C5	C1	C2	108.6(4)	O3	C41	C42	112(3)
C1	C2	Fe1	70.1(2)	O3A	C41A	C42A	132(2)

Table A.5 Selected Torsion Angles of compound **2**.

A	B	C	D	Angle/°	A	B	C	D	Angle/°
Fe1	C1	C2	C3	-60.3(3)	C12	C13	C14	C15	-0.8(4)
Fe1	C1	C5	C4	59.2(2)	C12	C13	C17	N1	148.2(3)
Fe1	C2	C3	C4	-60.2(3)	C13	C14	C15	C16	0.6(5)
Fe1	C3	C4	C5	-60.3(2)	C14	C13	C17	N1	-36.1(4)
Fe1	C4	C5	C1	-59.2(2)	C14	C15	C16	C11	0.8(5)
Fe1	C6	C7	C8	-59.2(2)	C16	C11	C12	C13	1.6(4)
Fe1	C6	C10	C9	59.7(2)	C17	N1	C18	C19	-76.4(4)
Fe1	C6	C10	C11	-120.6(3)	C17	N1	C35	C36	166.6(3)
Fe1	C7	C8	C9	-59.1(2)	C17	C13	C14	O1	2.7(5)
Fe1	C8	C9	C10	-59.3(2)	C17	C13	C14	C15	-176.7(3)
Fe1	C9	C10	C6	-59.4(2)	C18	N1	C17	C13	166.9(3)
Fe1	C9	C10	C11	120.8(3)	C18	N1	C35	C36	-72.5(4)
Fe1	C10	C11	C12	85.1(4)	C18	C19	C20	O2	1.3(6)
Fe1	C10	C11	C16	-95.7(3)	C18	C19	C20	C21	-177.9(4)
Fe2	C25	C26	C27	-60.3(3)	C18	C19	C24	C23	178.7(3)
Fe2	C25	C29	C28	59.2(2)	C19	C20	C21	C22	-1.1(7)
Fe2	C26	C27	C28	-59.2(3)	C20	C19	C24	C23	0.3(6)
Fe2	C27	C28	C29	-59.3(2)	C20	C21	C22	C23	1.0(7)
Fe2	C28	C29	C25	-58.9(2)	C21	C22	C23	C24	-0.3(6)
Fe2	C30	C31	C32	-59.2(3)	C21	C22	C23	C25	-179.2(4)
Fe2	C30	C34	C33	59.3(3)	C22	C23	C24	C19	-0.4(6)
Fe2	C31	C32	C33	-60.1(3)	C22	C23	C25	Fe2	-87.2(4)
Fe2	C32	C33	C34	-59.4(3)	C22	C23	C25	C26	1.0(6)
Fe2	C33	C34	C30	-59.1(3)	C22	C23	C25	C29	-177.4(4)

A	B	C	D	Angle/°	A	B	C	D	Angle/°
O1	C14	C15	C16	-178.8(3)	C23	C25	C26	Fe2	-119.4(4)
O2	C20	C21	C22	179.6(4)	C23	C25	C26	C27	-179.7(3)
N1	C18	C19	C20	-65.6(5)	C23	C25	C29	Fe2	120.1(4)
N1	C18	C19	C24	116.1(4)	C23	C25	C29	C28	179.3(3)
N1	C35	C36	N2	-13.1(5)	C24	C19	C20	O2	179.7(4)
N1	C35	C36	C37	167.5(4)	C24	C19	C20	C21	0.5(6)
N2	C36	C37	C38	-2.0(7)	C24	C23	C25	Fe2	93.9(4)
C1	C2	C3	Fe1	60.9(2)	C24	C23	C25	C26	-177.9(3)
C1	C2	C3	C4	0.7(4)	C24	C23	C25	C29	3.7(6)
C2	C1	C5	Fe1	-59.1(3)	C25	C23	C24	C19	178.5(3)
C2	C1	C5	C4	0.1(4)	C25	C26	C27	Fe2	60.2(2)
C2	C3	C4	Fe1	59.6(3)	C25	C26	C27	C28	1.0(4)
C2	C3	C4	C5	-0.6(4)	C26	C25	C29	Fe2	-58.5(2)
C3	C4	C5	Fe1	59.5(2)	C26	C25	C29	C28	0.6(4)
C3	C4	C5	C1	0.3(4)	C26	C27	C28	Fe2	58.7(3)
C5	C1	C2	Fe1	59.8(3)	C26	C27	C28	C29	-0.6(4)
C5	C1	C2	C3	-0.5(4)	C27	C28	C29	Fe2	58.8(2)
C6	C7	C8	Fe1	58.9(2)	C27	C28	C29	C25	0.0(4)
C6	C7	C8	C9	-0.2(4)	C29	C25	C26	Fe2	59.3(2)
C6	C10	C11	C12	174.8(3)	C29	C25	C26	C27	-1.0(4)
C6	C10	C11	C16	-6.0(5)	C30	C31	C32	Fe2	58.9(3)
C7	C6	C10	Fe1	-59.7(2)	C30	C31	C32	C33	-1.2(5)
C7	C6	C10	C9	-0.1(3)	C31	C30	C34	Fe2	-60.0(3)
C7	C6	C10	C11	179.7(3)	C31	C30	C34	C33	-0.7(4)
C7	C8	C9	Fe1	59.4(2)	C31	C32	C33	Fe2	60.2(3)

A	B	C	D	Angle/°	A	B	C	D	Angle/°
C7	C8	C9	C10	0.2(4)	C31	C32	C33	C34	0.8(5)
C8	C9	C10	Fe1	59.4(2)	C32	C33	C34	Fe2	59.1(3)
C8	C9	C10	C6	-0.1(3)	C32	C33	C34	C30	0.0(4)
C8	C9	C10	C11	-179.8(3)	C34	C30	C31	Fe2	60.4(3)
C9	C10	C11	C12	-5.5(5)	C34	C30	C31	C32	1.2(4)
C9	C10	C11	C16	173.7(3)	C35	N1	C17	C13	-71.5(4)
C10	C6	C7	Fe1	59.4(2)	C35	N1	C18	C19	161.8(3)
C10	C6	C7	C8	0.2(4)	C35	C36	C37	C38	177.4(4)
C10	C11	C12	C13	-179.2(3)	C36	N2	C40	C39	0.6(7)
C10	C11	C16	C15	178.9(3)	C36	C37	C38	C39	0.8(8)
C11	C12	C13	C14	-0.3(4)	C37	C38	C39	C40	0.9(8)
C11	C12	C13	C17	175.6(3)	C38	C39	C40	N2	-1.6(8)
C12	C11	C16	C15	-1.9(4)	C40	N2	C36	C35	-178.1(4)
C12	C13	C14	O1	178.5(3)	C40	N2	C36	C37	1.3(6)